(NASA-CR-170754) SPECTROPHOTOVOLTAIC ORBITAL POWER GENERATION Final Report, Aug. 1981 - Nov. 1982 (Honeywell Systems and Research) 82 p HC A05/MF A01 CSCL 10B
N83-25040
Unclas
G3/44 03685

83SRC22

SPECTROPHOTOVOLTAIC ORBITAL POWER GENERATION

(PHASE III)

FINAL REPORT

MARCH 31, 1983

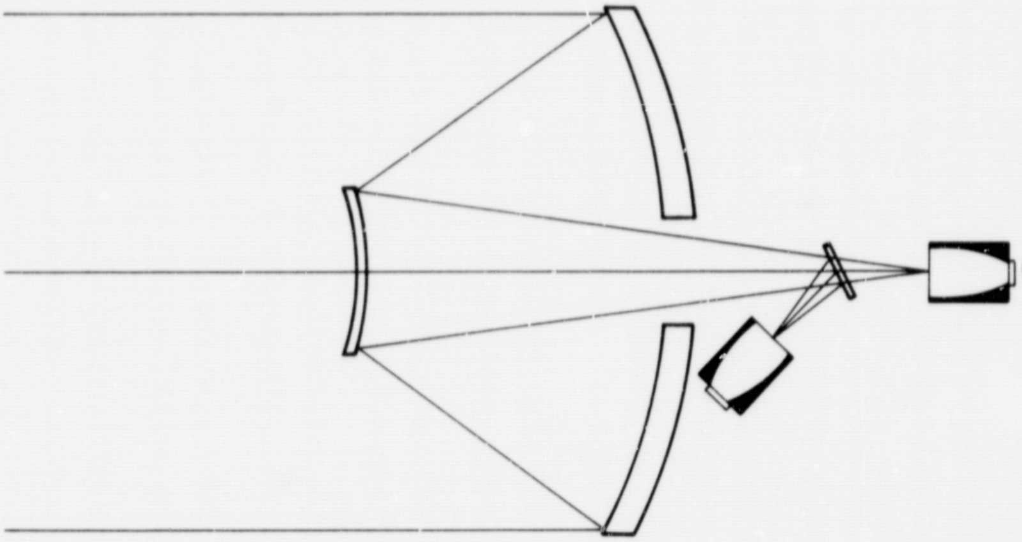

for
GEORGE C. MARSHALL SPACE FLIGHT CENTER
Contract NAS 8-33511
by

Honeywell

Systems and Research Center
2600 Ridgway Parkway
P.O. Box 312
Minneapolis, MN 55440

CONTENTS

Section Page

i, ii

LIST OF ILLUSTRATIONS

LIST OF ILLUSTRATIONS (continued)

LIST OF ILLUSTRATIONS (concluded)

LIST OF TABLES

SECTION 1

INTRODUCTION AND SUMMARY

This is the final report for work performed under Contract NAS8-33511 by the Honeywell Systems and Research Center for NASA's George C. Marshall Space Flight Center, Huntsville, Alabama. This is the third phase of this contract. The work in this and previous phases of the contract is summarized below.

SUMMARY OF PHASE I

During Phase I of the program, a spectral splitting photovoltaic concept was defined. In this concept, the energy spectrum is split into different bands in which photon energy is effectively converted into electrical energy via photovoltaic cells that have matching spectral responses. The efficiency of the system also increases with the concentration ratio if the temperature of the cell is maintained constant ~300K. Assuming this condition was met, a system with 1000:1 concentration ratio was defined, using a Cassegrain telescope as the first-stage concentration (270 x), and compound parabolic concentrators (CPC) for the second-stage concentration of 4.7 x for each spectral band. Using reported state-of-the-art solar cell parameters and considering losses due to optics and beamsplitters, the calculated efficiencies of one- to four-cell systems varied from ~22% to ~30%. When the cost of optics, beamsplitter, radiator, and the cost of developing new cells are considered, the most cost-effective system was the two-cell gallium arsenide/silicon (GaAs/Si) system.

The advantages of the spectrophotovoltaic (SPV) concept are: 1) the increase in photoelectric conversion efficiency without development of new materials and cells; 2) intrinsic particle radiation hardness, since the cells are not directly exposed to particle radiation; and 3) intrinsic resistance to laser damage, since the acceptance angle of the concentrator system is only ±0.5°, pointing at the sun. Thus, the spectrophotovoltaic concept is especially suitable for space power generation.

SUMMARY OF PHASE II

In Phase II of the program, the objective was to define and design a subscale model which would demonstrate the hardware feasibility of selected components of the full-scale spectrophotovoltaic orbital power generation system up to a concentration ratio of 1000:1. The design for ground-based testing would be in sufficient detail to produce a subscale model capable of demonstrating the performance characteristics of the major components and the integrated system.

The subscale model defined was a 10-in. aperture system with an effective concentration ratio up to 1000:1, similar to that defined in Phase I. The partially concentrated solar spectrum was divided into two bands by a beamsplitter and then focused onto two selected cells. The chosen cells were well-developed GaAs and Si solar cells. Both reflective and transmitting mode to GaAs (denoted by GaAs/Si and Si/GaAs, respectively) would be tested, since each configuration had its own merits. The model would demonstrate the high conversion efficiency, due to both spectrum splitting and high concentration ratio of the defined concept. In addition, thermal data on various system components would be taken; these data would shed light on system losses and thus lead to an optimal design. The ability of the system components to withstand such high concentration would also be tested.

The optical design for the subscale model was a scaled-down version of the Phase I design with an increase of the back focal length from 3 in. to 6 in. to allow room for thermal measurement at the CPC solar cell closest to the primary. This caused the secondary obscuration to increase from 7% to 10%. Three manufacturing methods for the optical components were explored. Among these, electroforming, a version of electroplating, was the most economical for the CPCs. Diamond turning and conventional glass grinding appeared best for the primary and secondary. Optical tolerance analysis of the mirror included three other mirror combinations. The most critical alignment was the separation between the primary and secondary mirrors, which had to be maintained within ±0.015 in.

PHASE III OBJECTIVES AND SUMMARY

The objective of building and testing the subscale model of the spectrophotovoltaic system was to demonstrate the efficiency gains attainable by splitting the spectrum and directing the energy to spectrally matched solar cells and to take advantage of cell efficiency gains resulting from operating at high solar concentration ratios.

The test results presented in this report show that there is a small advantage to be gained by implementing the spectrophotovoltaic concept. Component performance contributed to lower than anticipated system efficiency. The highest measured system efficiency was 14.2%, with the GaAs cell contributing 12% and the Si cell contributing 2.2% of the total conversion efficiency.

Measured and manufacturers' data on all of the components were input to a computer model of the system. Good agreement was found between the measured and calculated parameters for the GaAs solar cell. The model and computer printout are given in Appendix A.

SECTION 2

DESIGN

The objective of the design was to provide a solar concentrator for testing solar cells under very high concentration ratios while employing spectral beamsplitting to increase the net solar to electrical energy conversion efficiency. In addition, the subscale test model would closely model the optical features of the concentrator concept designed in Phase I of this contract.* Additional requirements on the test model were that it be large enough to provide readily measurable electric and thermal output from each solar cell. The upper limit on model size was constrained by the need for portability and by component costs.

The optical design only required one departure from linear scaling. To provide more clearance between the back of the primary mirror and the solar cells and for instrumentation and thermal insulation, the back focal length of the optics was increased slightly. This required a larger diameter secondary mirror with an accompanying increase in obscuration from 7.3% to 10%. Figure 1 is a cross-sectional drawing which identifies the optical components.

---

*Although the Phase I design considered only a single concentrator system with a 100 kW electric output, the optimum aperture size for most efficient fabrication and energy conversion is not clear. Each size of concentrator will require different manufacturing techniques, alignment tolerances, and materials to achieve an optimum design. Determining the best solution will require a series of complete system designs.

ORIGINAL PAGE IS
OF POOR QUALITY

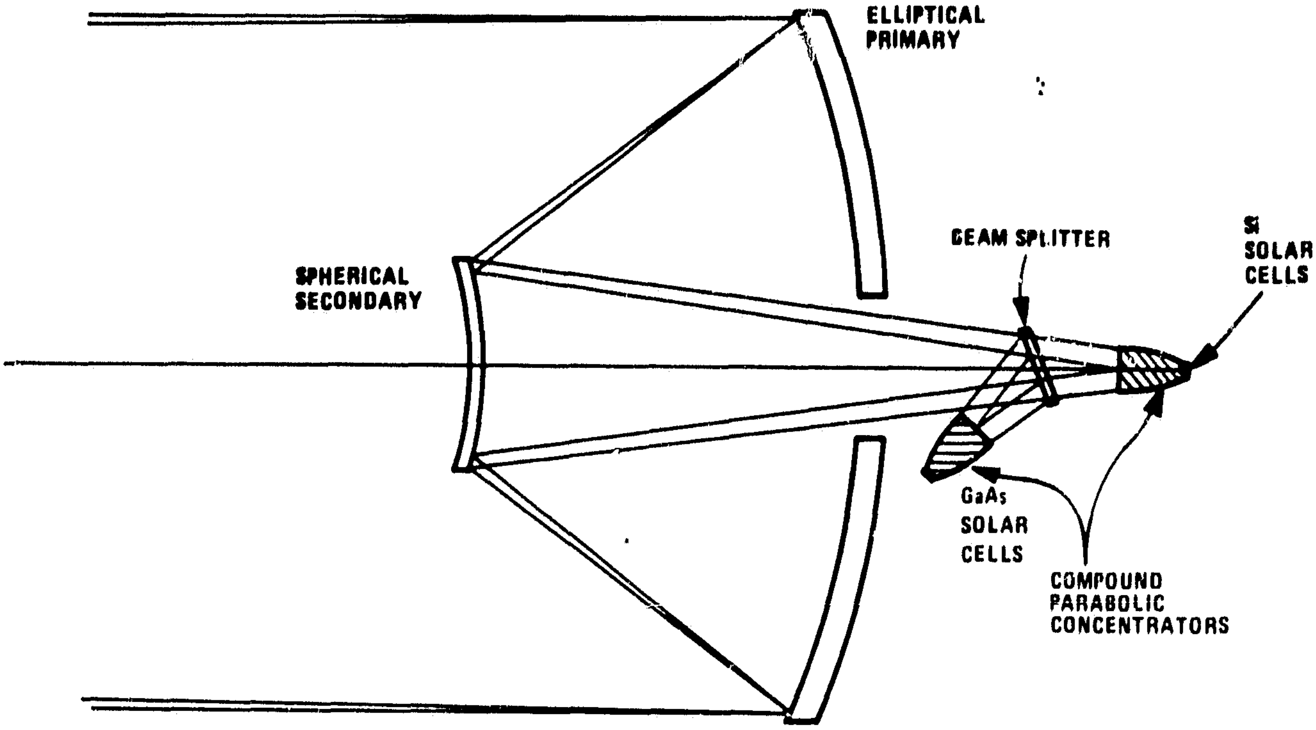

Figure 1. f/3.5 Optical System

The double-width rays trace out the path of rays originating from the edges of the 0.5° wide sun. The beamsplitter is placed at a 22.5° angle to the optical axis to redirect the short wavelength portion of the spectrum to the solar cell having the higher bandgap. The longer wavelength portion of the spectrum passes through the beamsplitter to the lower bandgap solar cell.

The optical concentration at the aperture of the compound parabolic concentrator is approximately 270:1, and an additional concentration of 4.66 occurs in the CPC for a total concentration of 1256:1. Obscuration losses due to the secondary mirror surfaces bring the net concentration down to approximately 1000:1.

This particular optical configuration was the result of an optimization study performed in Phase I of the contract. The tradeoffs considered surface accuracy requirements, space deployment concepts, beamsplitter heat loads, and cell-to-beamsplitter geometry. The results were that the most economical system performed the solar concentration in two stages, as shown, using an f/3.5 primary concentrator and a CPC secondary concentrator.

Table 1 summarizes the subscale model optical design parameters. The characteristic optical surface radii, focal lengths and separations, and the theoretical concentration ratios are listed. The tradeoffs and rationale for selecting a 10-in. aperture design were presented in the Phase II design study report. The main driving issues were that a 10-in. aperture was large enough to collect easily measured quantities of energy, while being small enough to be easily portable and have minimum component costs.

Figure 2 is a cross-sectional cutaway view of the subscale test model showing the physical size, shape, and layout of various optical components. The primary is an f/0.7 diamond-turned elliptical mirror made from aluminum. The secondary is a spherical quartz mirror bolted to the spider mount, the two together forming what is referred to as a Dall-Kirkham telescope system. The beamsplitter is a multilayer coating deposited on Infrasil (fused quartz) substrate. It is mounted in an aluminum holder which is turn is bolted to the primary mechanical structure of the concentrator. The two solar cells and CPCs are each mounted in their own separate housing which provides the mechanical support and thermal insulation. Electric power leads, thermocouples, and coolant lines are also supported by the solar cell mounts. Complete detailed mechanical drawings of the various components are provided in Appendix B.

TABLE 1. SYSTEM DESIGN PARAMETER FOR SUBSCALE MODEL

Primary Diameter = 10.0"

Primary Focal Length = 7.0"

Primary F/# = 0.70

Secondary Magnification = 5.0

System Back Focal Length = 6.0"

Source Angular Subtense = ± 0.5°

System Focal Length = 35.00

System F/# = 3.50

Secondary Focal Length = -2.71"

Secondary Diameter = 3.18"

Primary-Secondary Separation = 4.83"

Secondary Obscuration = 0.10

Obscuration Efficiency = 0.90

CPC Entrance Aperture Dia. = 0.61"

Concentration of Cassegrain = 269.63

Solar Cell Diameter = 0.28"

Concentration of CPC = 4.66

Length of CPC = 0.85

System Concentration = 1256

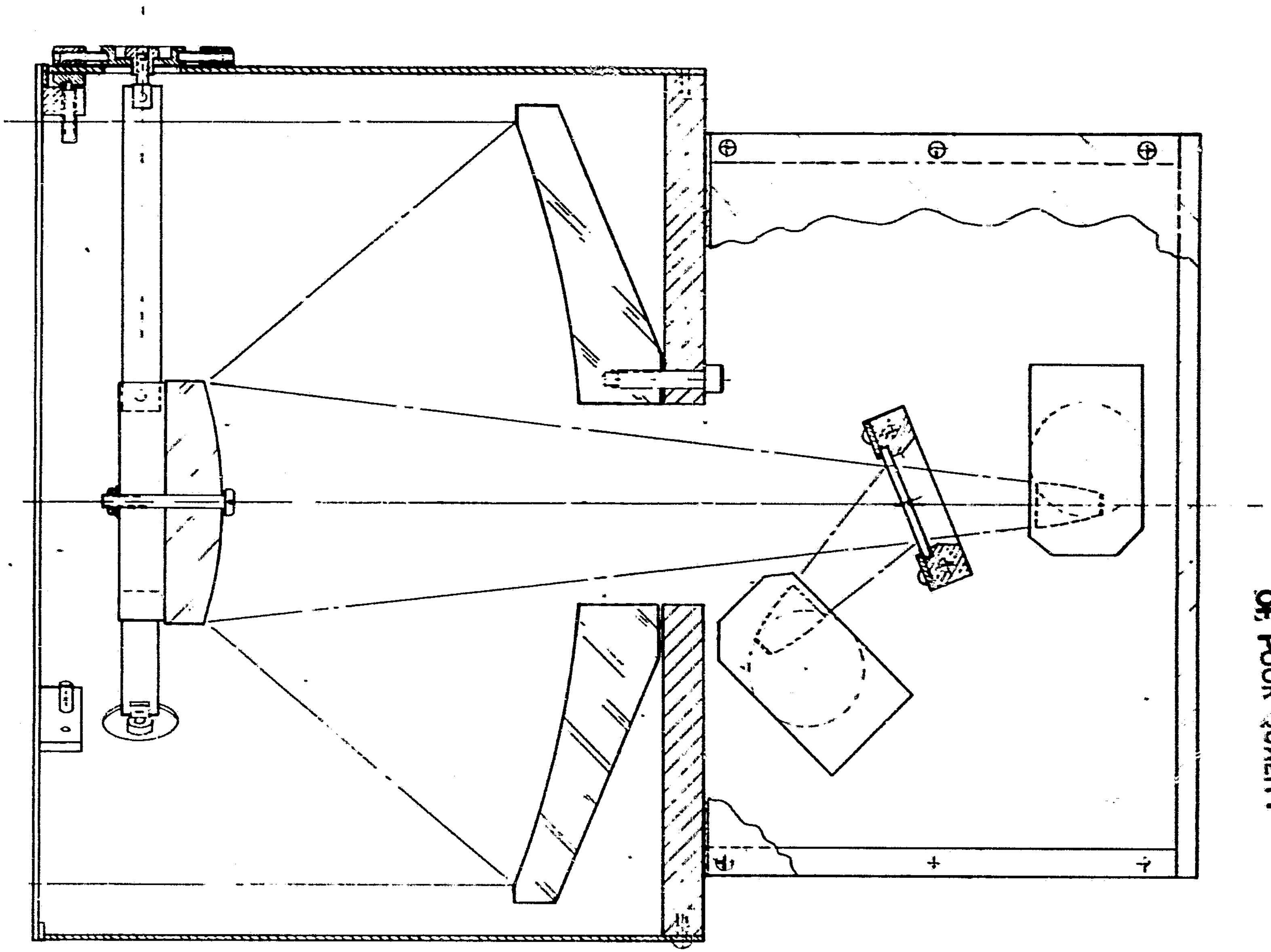

Figure 2. Subscale Test Model Cutaway

Figure 3 is a photograph of the assembled mechanical structure, tracking drive, and data logger. It shows the mounting relationship of the test model, two Epply normal incidence pyrheliometers, and the drive mechanism. Two adjustable counterweights are provided to minimize the unbalanced loads both on the declination adjustment and the polar rotation axis. The drive mechanism is a standard Epply pyrheliometer drive modified to accept the greater weight and higher center of gravity of the test model. All components are either anodized aluminum, stainless steel, or plexiglass except for the drive mechanism, which is baked enamel on steel.

The data logger used for recording the cell current, voltage, temperatures, and solar intensity was a 30-channel Fluke Model 2240C data logger having a 40,000-count dual-slope integration. It was capable of resolving differences of 1 mV or 1 part in 40,000, whichever is larger. Temperature measurements were resolved to 0.1°C.

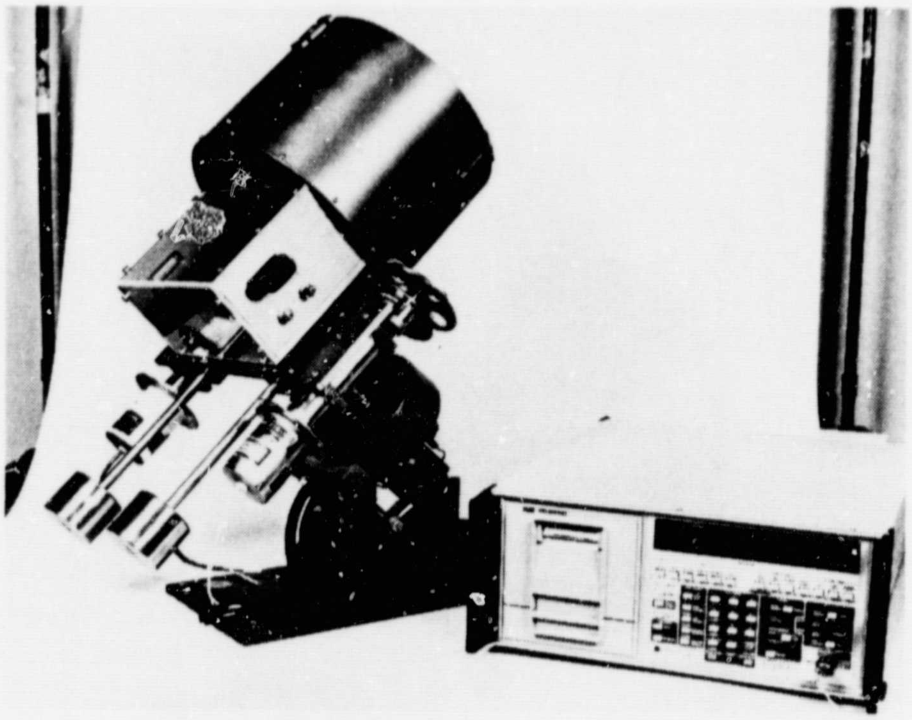

Figure 3. Subscale Test Model, Mount, and Data Logger

Figure 4 is a close-up view of the back of the test model showing the beamsplitter mount, the CPC and cell holders, and the electric signal and coolant feedthroughs. The CPC/cell holders are bolted to the mounting plate with single bolts placed in oversized holes to permit rotation and translation for the fine alignment. Height adjustment was provided by shims. (In the final assembly, no shimming was required to achieve optical alignment.) The back and top of the cell mounting compartment was covered with plexiglass to reduce convection losses and dust contamination of the intensely illuminated optical components. The dust covers are shown installed in Figure 3 but are removed in Figure 4.

Figure 5 shows the assembled concentrator while it was being tested in sunlight. The cabling so predominate in the photograph consists of voltage and current leads for each solar cell, thermocouples, pyrheliometer leads, tracker drive power, and cell coolant lines. The coolant used was water with approximately 15% alcohol to prevent freezing.

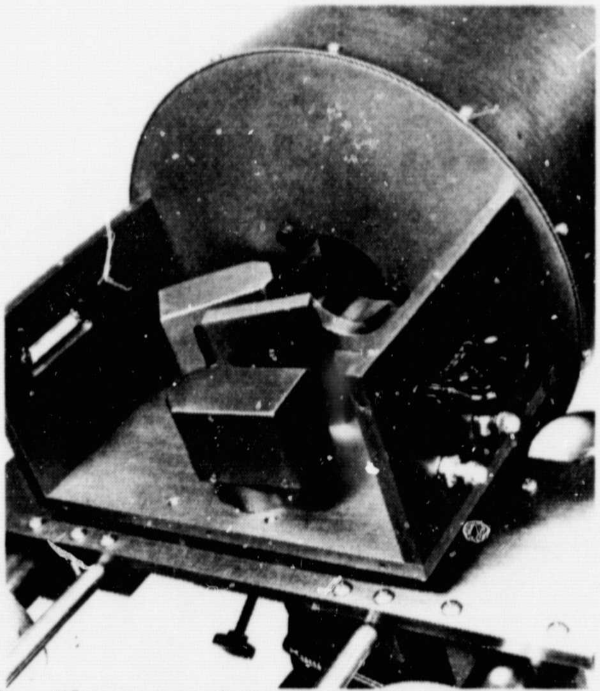

Figure 4. Close-Up of Test Model Solar Cell Mounts

Figure 5. Subscale Test Model During Outdoor Testing

Preliminary alignment of the concentrator to the sun was performed using the pinhole and target alignment sight on the pyrheliometers. Fine alignment was performed by fine adjusting the declination and hour angles to maximize the short-circuit current from each or the solar cells.

The one-degree field of view of the concentrator while tracking a half-degree wide sun provided an acceptably wide margin of error such that once aligned, the concentrator would track for an hour or more without requiring fine adjustment. Improving the alignment of the polar axis to the earth axis would have increased this accurate tracking time to several hours. Measurements and geometric calculations showed that the pyrheliometers were very insensitive to alignment errors of ± 1°. Hence, the concentrator-to-pyrheliometer alignment did not have to be changed with small adjustments of the concentrator to sun alignment.

In the following section, the numerical modeling performed during this program will be discussed. Test data measured for various components and the system performance will be presented in Section 4.

SECTION 3

MODELING

INTRODUCTION

Evaluation of the test model required an analytic model for performance comparison and predictions. A detailed analytic model of the concentrator was created by spectrally integrating the component performance data. Spectral measurements of component reflectance, transmission, and conversion efficiency were made for each component and integrated with the solar spectral intensity within the 0.29- to 1.1-μm spectral range. The conversion efficiency is the quotient of electrical output divided by solar energy input. In the following paragraphs, all of the parameters which went into the analysis will be discussed, starting from the solar spectral data and ending with the predicted performance.

SOLAR SPECTRAL DATA

The solar spectral data used in this analysis were taken from a 1978 paper by Mecherikunnel and Richmond.[1] This paper presents spectral irradiance data over the wavelength range 290 to 4000 nanometers (0.29 to 4.0 μm) for air masses 0 to 10 (AM0 to AM10). (For sea-level observations the air mass is approximately $1/\sin\theta$, where θ is the altitude angle of the sun.)

The paper further presents correction factors for various levels of atmospheric moisture, ozone, and turbulence. In all of the following analyses, it was assumed that the atmosphere was clear, with Angstrom turbidity coefficients $\alpha = 0.66$ and $\beta = 0.170$, 20 mm of precipitable water vapor and 3.4 mm of ozone.

Figure 6 is a plot of solar spectral irradiance for AMO and an AM2 spectrum with the atmospheric conditions given above. The atmospheric attenuation is stronger at the shorter wavelengths but shows very strong water-absorption bands at the longer wavelengths. The overall effect on a two-color photovoltaic conversion system is to shift a greater percentage of the energy from the shorter wavelength solar cell to the longer wavelength cell. A system optimized for space applications will not have the maximum efficiency when tested at AM2 conditions.

Atmospheric attenuation can be minimized by testing at higher altitudes and when the sun is most nearly overhead. Figure 7 is a plot of apparent air mass as a function of solar zenith angle and test-site elevation. The test sites plotted include several high-altitude observations plus Minneapolis, and Leadville, Colorado. Table Mountain, California, provides the best compromise in terms of accessibility, working facilities, and reduction in air mass.

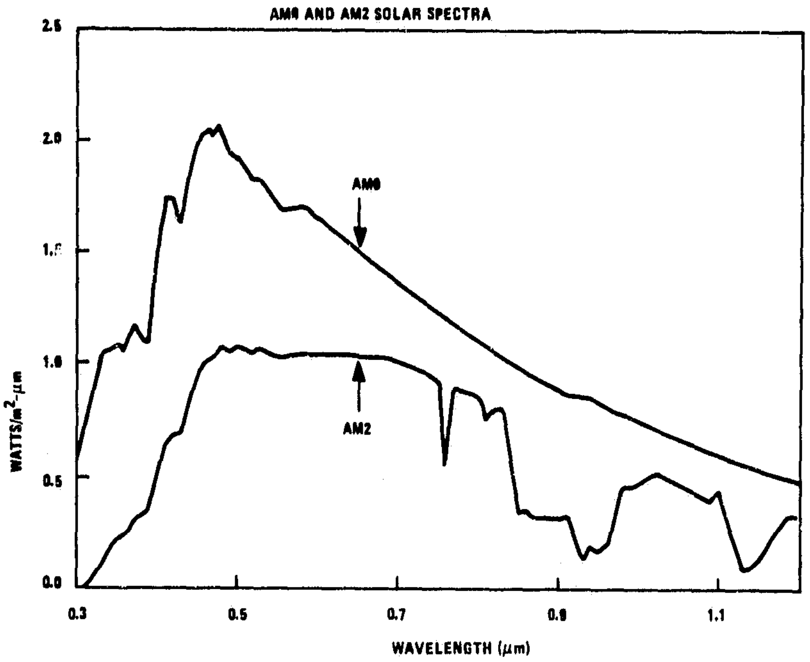

Figure 6. Solar Spectral Intensity Distribution

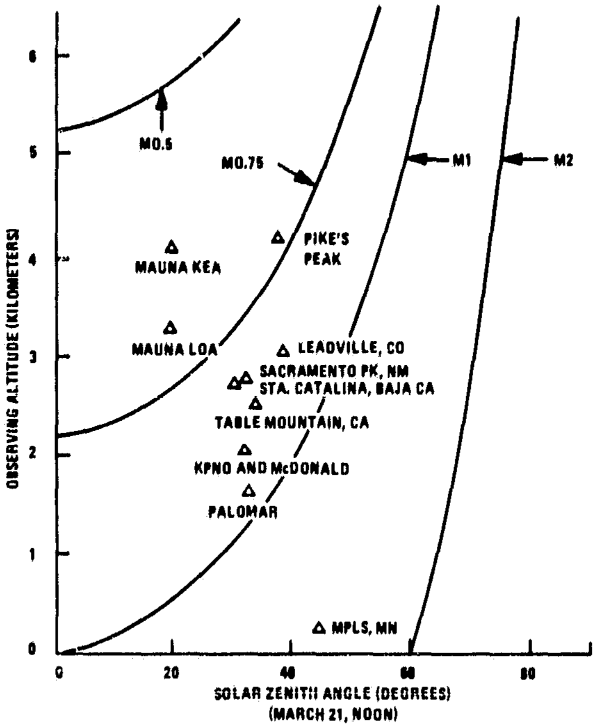

Figure 7. Air Mass for Various Test Sites

In all of the following analyses the air mass and turbidity assumed was that for average clear sky conditions with either an AM1 or AM2 condition. Should further testing be performed, testing at a high-altitude site such as Table Mountain would be recommended.

CONCENTRATOR COMPONENT PROPERTIES

Introduction

Before the performance of the spectrophotovoltaic system can be predicted, the performance of each of its components must be characterized. The SPV concentrator system has a large number of components in the optical path, all of which impact the net conversion efficiency. Figure 8 is a cross-sectional drawing of the concentrator showing the relative size and

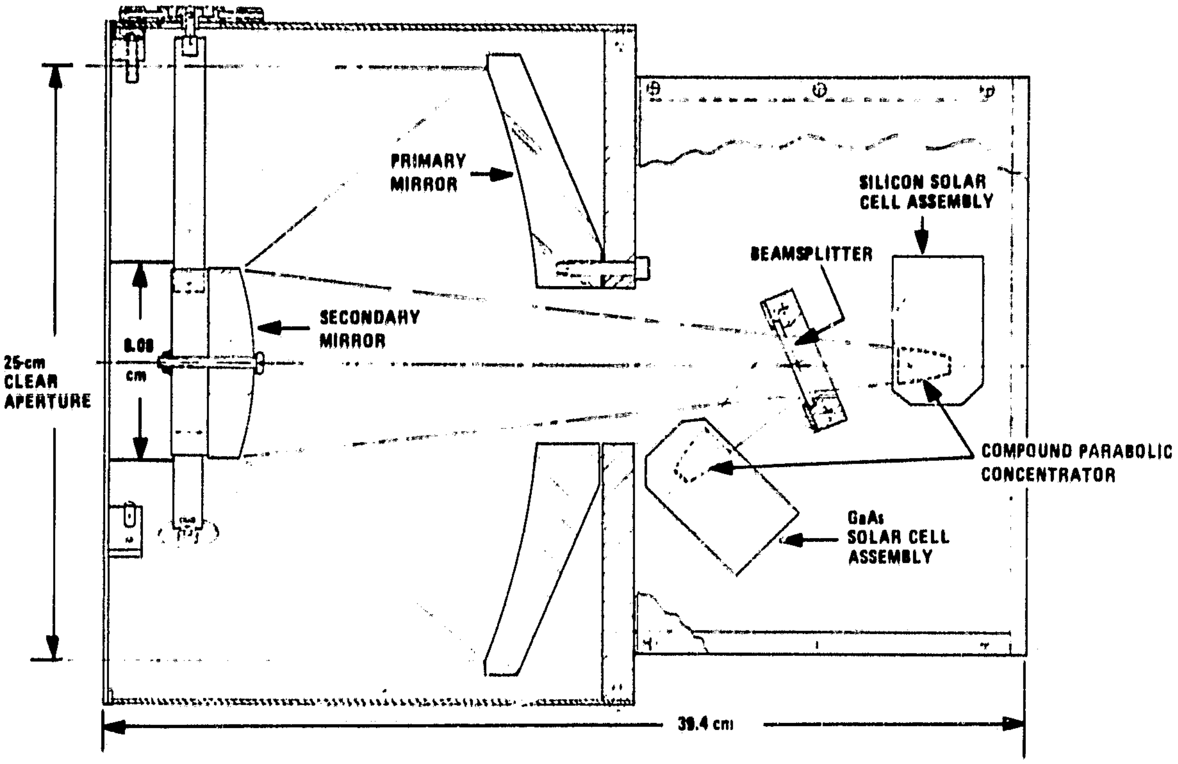

Figure 8. Spectrophotovoltaic Concentrator Layout

locations of the mirrors, beamsplitter, compound parabolic concentrators, and solar cells. Figure 9 provides the critical geometric dimensions of all the components in the optical system. In the following paragraphs the optical properties data for each of the components will be presented.

Mirrors

The primary and secondary mirror system together form what is known as a Dall-Kirkham telescope. The primary is an elliptical diamond-turned aluminum mirror; the secondary is a spherical quartz mirror. Both mirrors are overcoated with silver for maximum short-wave reflectance. Figure 10 is a plot of reflectance versus wavelength for a witness coupon overcoated with silver at the same time as the primary mirror. The integrated average solar reflectance (AMO) over the 0.4- to 1.1-μm spectral range was 86%. This

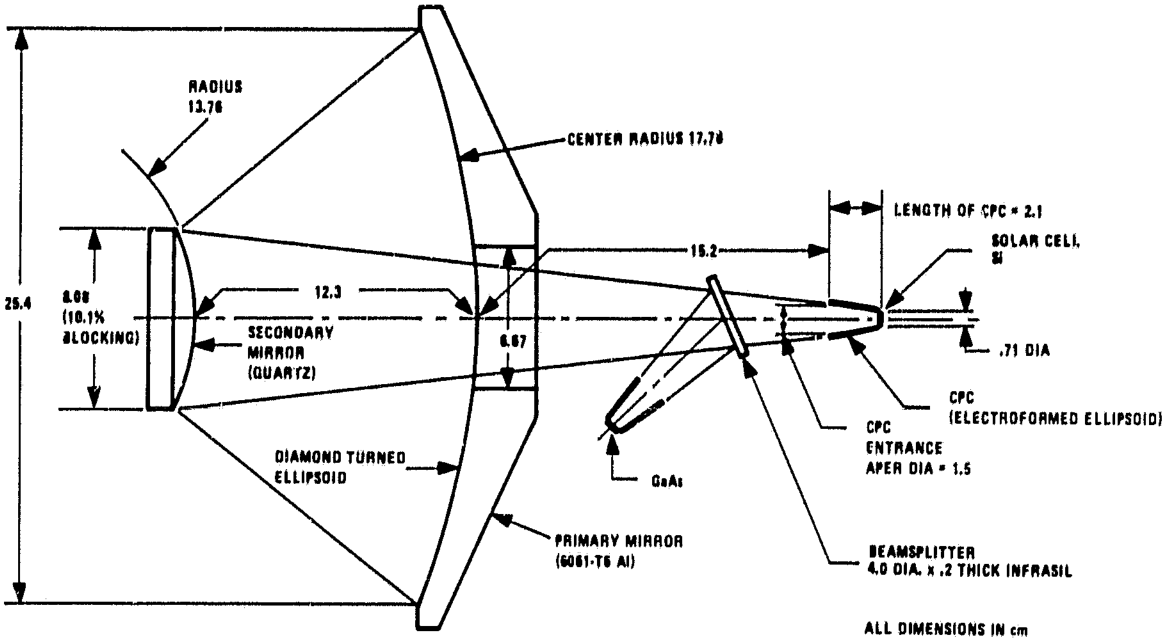

Figure 9. Concentrator Component Geometry

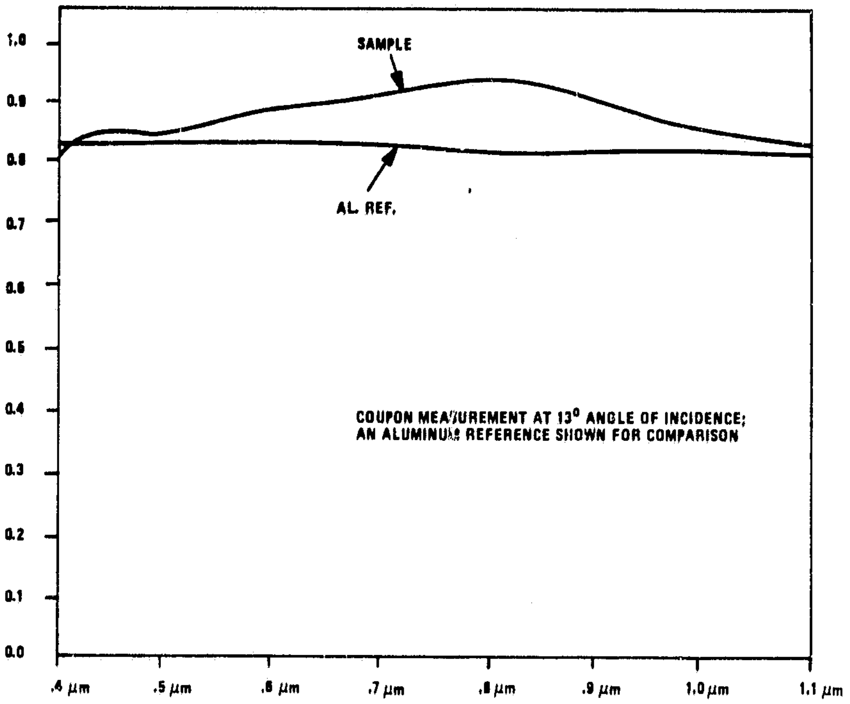

Figure 10. Primary Mirror Reflectance (coupon measurement at 13° angle of incidence; an aluminum reference shown for comparison)

would increase slightly for an AM2 spectrum because of the higher reflectance at longer wavelengths. An accurate reflectance measurement from a large, steeply curved mirror is difficult to perform. An approximate measurement of reflectivity was made using a double bounce technique as illustrated in Figure 11A and B. The reflectance measured at 0.63 μm was 0.86 ± 0.02 per surface. The large uncertainty was due to the relatively small detector collection aperture of the detector and the amount of surface scattering from the diamond-turned primary mirror. It is suspected that, had a larger aperture detector been available, the measured reflectance would have approached the 90% shown in Figure 10 ($\lambda = 0.63$ μm). The measurement scheme shown in Figure 11 had an acceptance angle of approximately 0.2°, whereas the acceptance angle of the solar cell is near 1°. In calculating the mirror reflectance it was assumed that the primary and secondary had the same reflectance. From a practical standpoint, it makes no difference whether one mirror has 100% reflectance and the other 74% or whether they both have 86%. From the limited amount of data available, the latter case appears to be a good approximation.

The reflectance requested from the vendor was 98% or greater over the 0.45- to 1.1-μm range. Coatings of this high reflectance and broadband are commercially available (Figure 12), without pushing the state-of-the-art. Increasing the reflectance of each mirror from 86% to 98% would increase the system conversion efficiency by 29.9%.

Beamsplitters

The spectral beamsplitter is the unique feature of this solar electric conversion system. Solar cells characteristically have a very steep long-wave cutoff (Figure 13). Since the solar cells having shorter wavelength cutoff characteristics operate at higher voltages, the electric power output is maximized by splitting the solar spectrum and directing portions of the spectrum to the spectrally matching solar cells.

ORIGINAL PAGE IS
OF POOR QUALITY

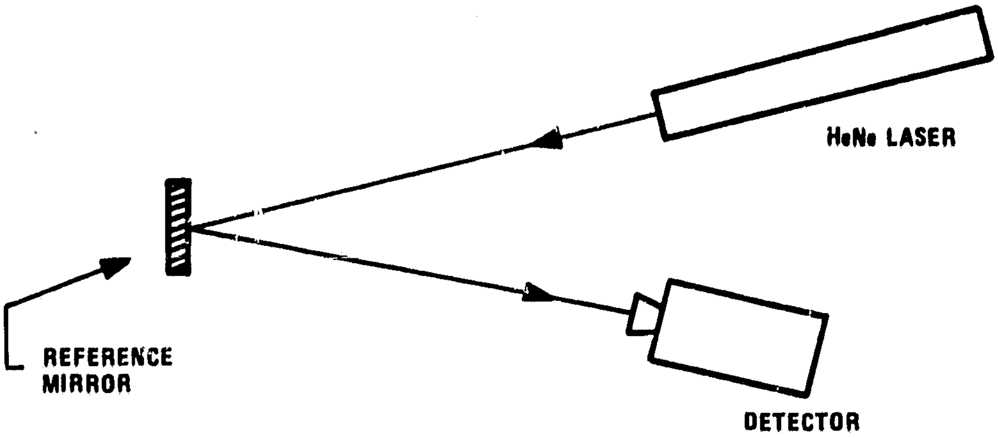

Figure 11A. Reference Mirror Calibration

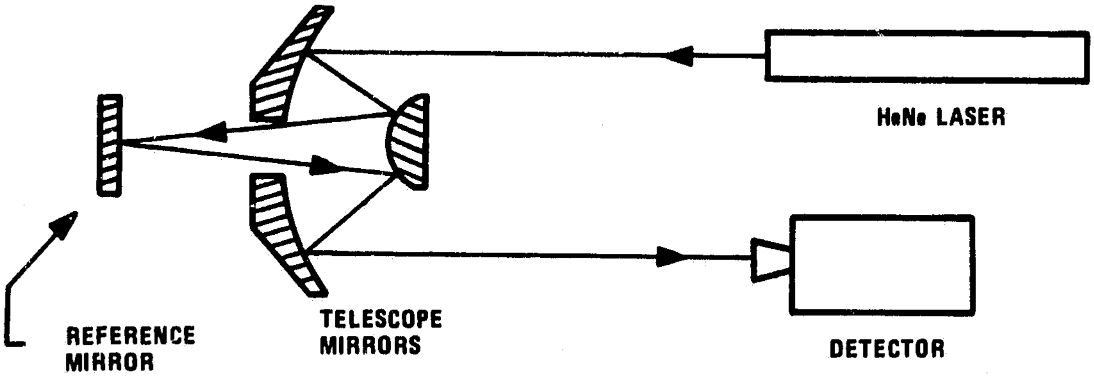

Figure 11B. Telescope Mirror Reflectance Measurement

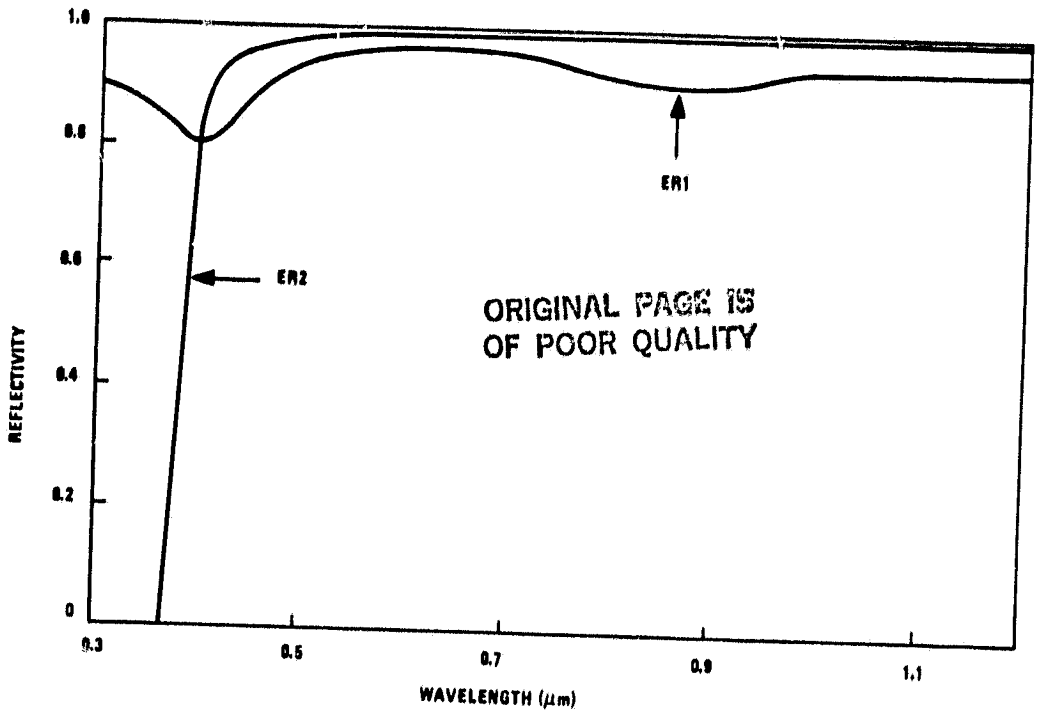

Figure 12. Newport Research Corporation Reflective Coatings

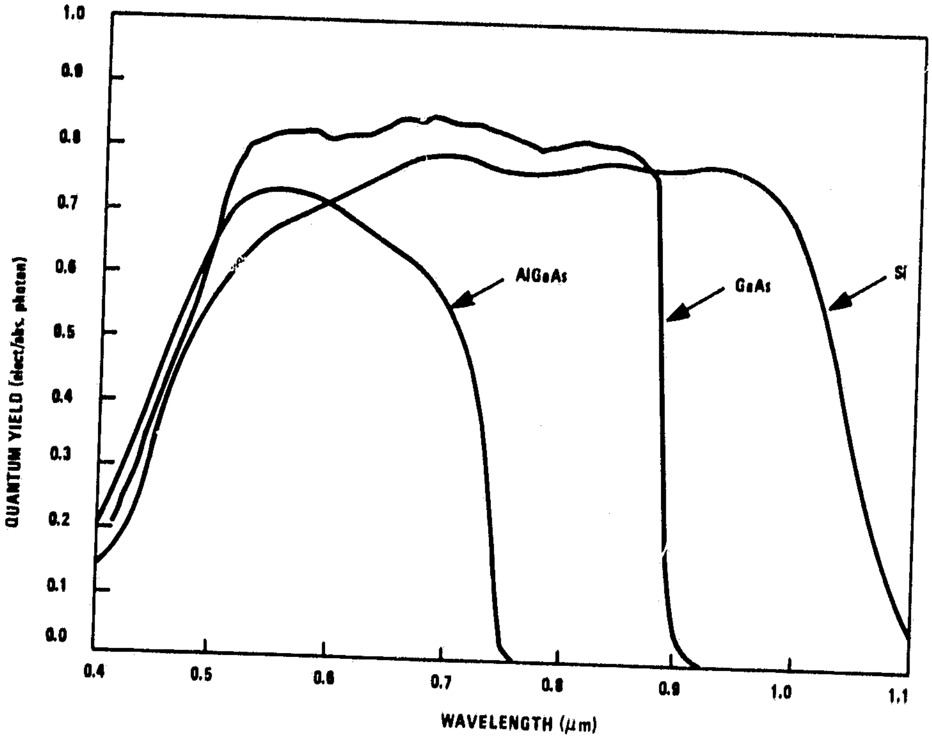

Figure 13. Solar Cell Quantum Efficiency Comparison

To determine the sensitivity of the conversion efficiency to the cutoff wavelength of the beamsplitter, a series of calculations were made for GaAs and Si cells using both AMO and AM2 solar spectra. Figure 14 shows a plot of efficiency versus beamsplitter cutoff wavelength. The curves indicate that the cutoff wavelength can vary ± 0.3 μm with less than a 5% reduction in net electrical power output. In the modeling an assumption was made that the reflected portion of the spectrum was totally reflected, and 1% of the remainder was absorbed. Depending on whether the short-wave portion of the spectrum, which contains more than 70% of the energy, was reflected or transmitted, the peak of the efficiency curve is shifted slightly. Since more energy is produced by the GaAs cell than by the Si cell, the system efficiency is slightly higher with a short-wave reflective beamsplitter.

Two sets of beamsplitters were purchased from Broomer Research, Inc.--one set for the AlGaAs/Si solar cell combination, and one for the GaAs/Si cell combination. Figures 15 and 16 show the GaAs/Si beamsplitter transmission and reflectance, respectively. Figure 17 shows the effect of turning the multilayer coated mirror over and measuring reflectance with the glass side toward the incident beam. The presence of harmonics in one orientation and not in the other is the result of the walk-off of the multiply reflected beam from the collection aperture of the spectrometer. The total reflectance is the sum of an infinite series of reflections, but since the spectrometer beam strikes the sample of an 8° angle the multiple reflections between the front and back surfaces are displaced from the principal reflection and do not reach the detector.

Figure 18 diagrams the reflection of the beam striking the surface at an angle. The total reflection from the beamsplitter is the infinite sum of the multiple reflections, given by the following equation:

$$\overline{R} = \frac{R_1 - 2R_1R_2 + R_2}{1 - R_1R_2} \tag{1}$$

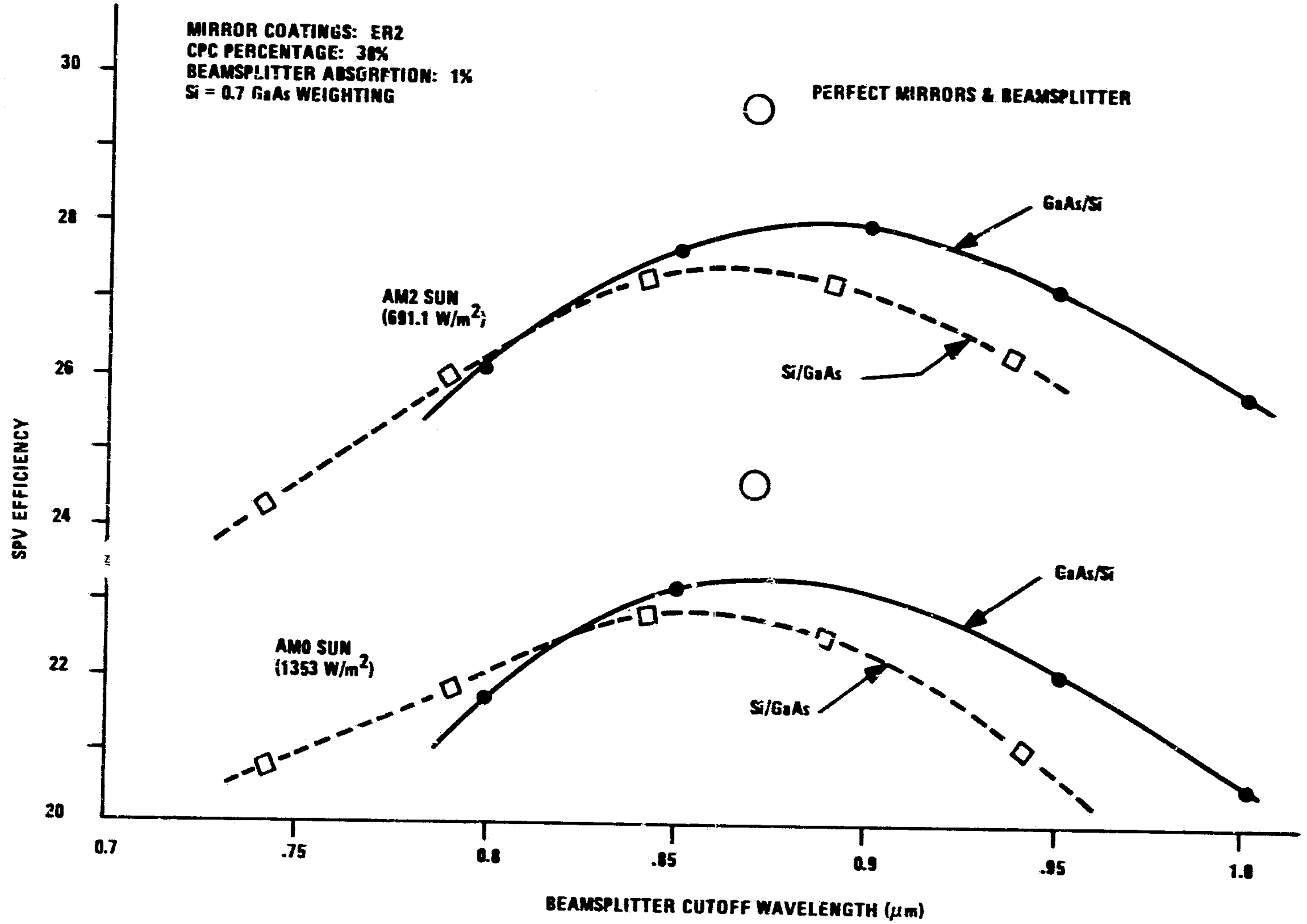

Figure 14. Calculated System Efficiency as a Function of Beamsplitter Cutoff

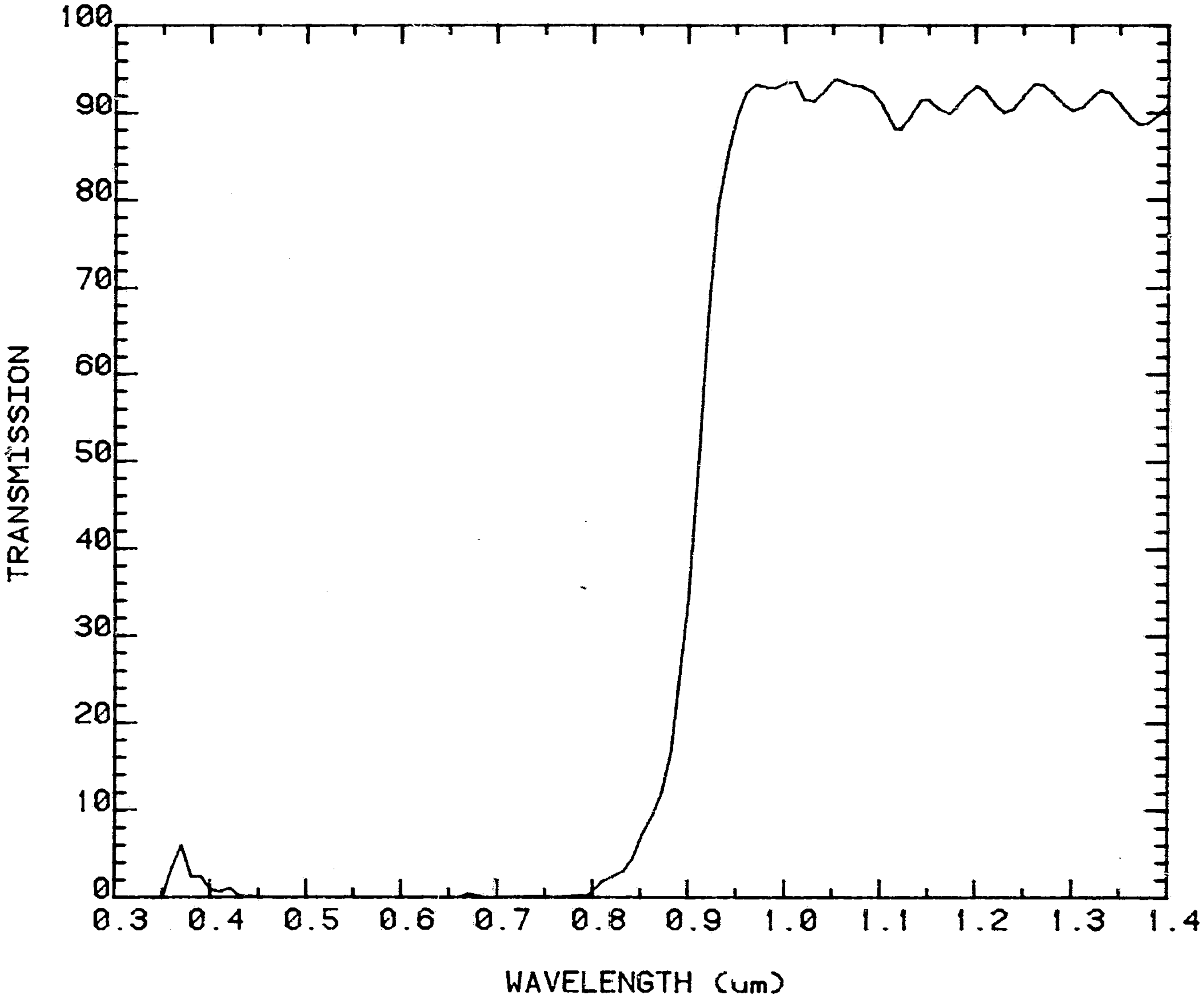

Figure 15. Measured Beamsplitter Transmission (22.5°, BS #1)

ORIGINAL PAGE IS
OF POOR QUALITY

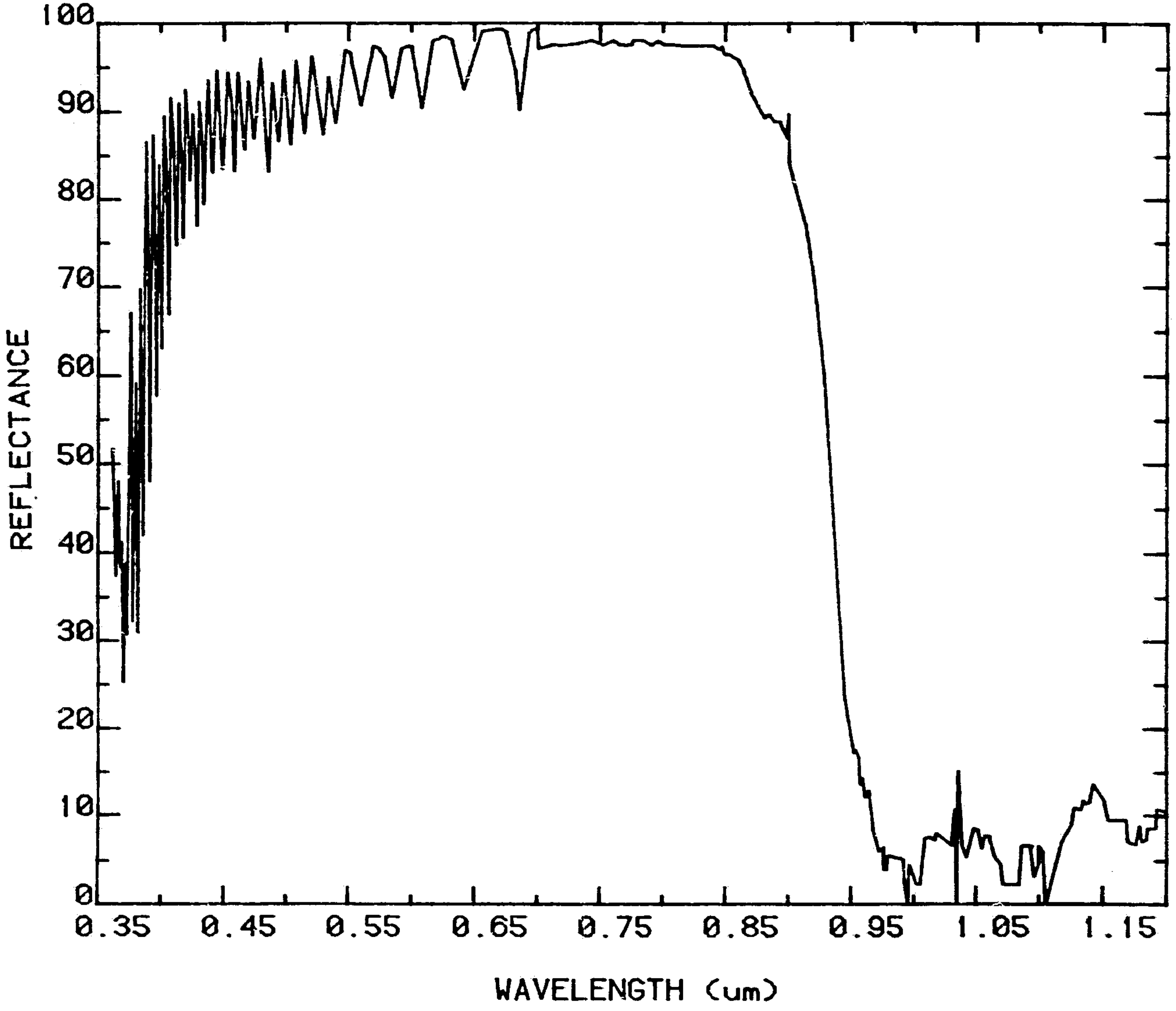

Figure 16. Beamsplitter Reflectance (Coating Side Toward Beam, BS #1)

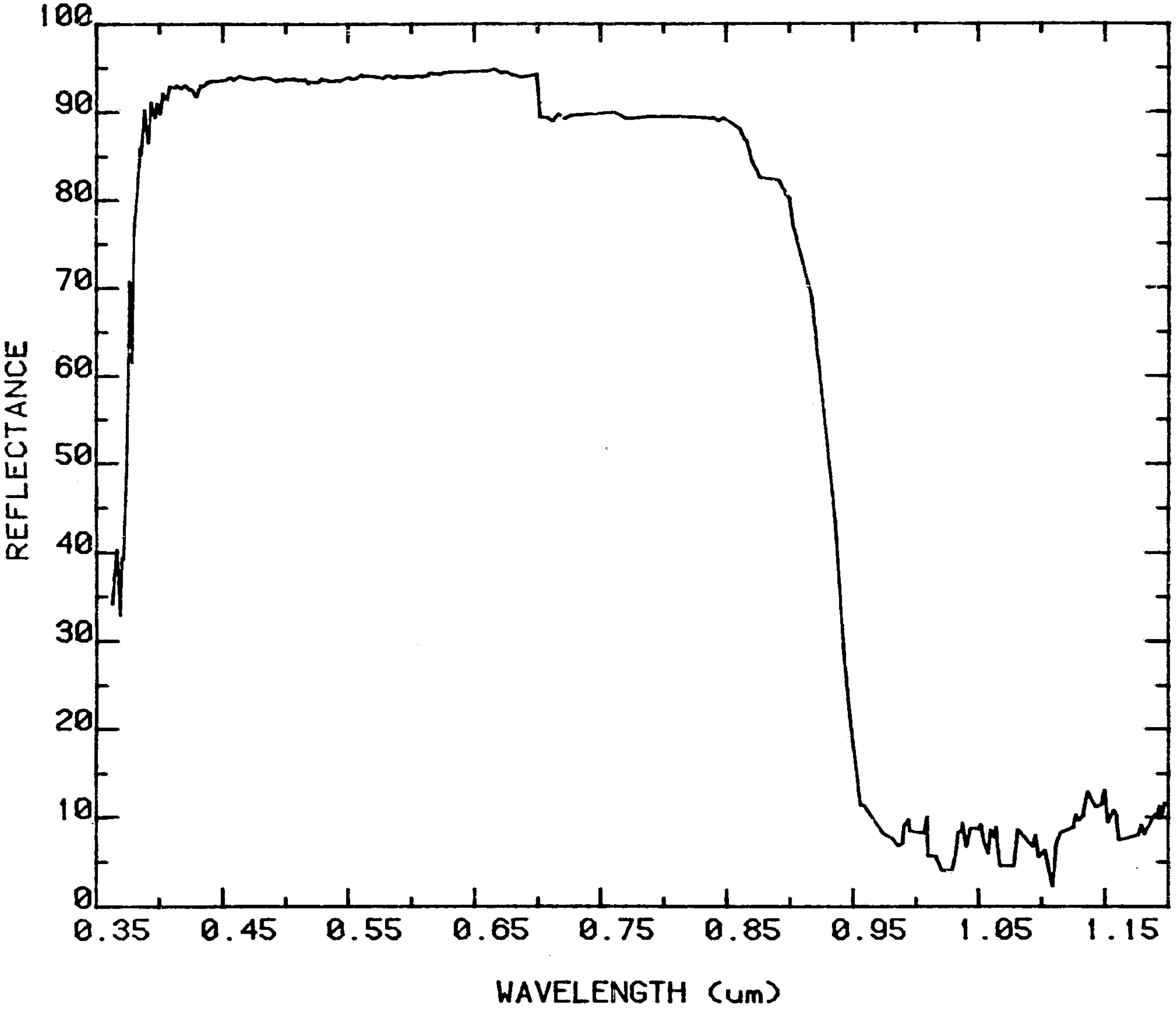

Figure 17. Beamsplitter Reflectance (Glass Side Toward Beam, BS #1)

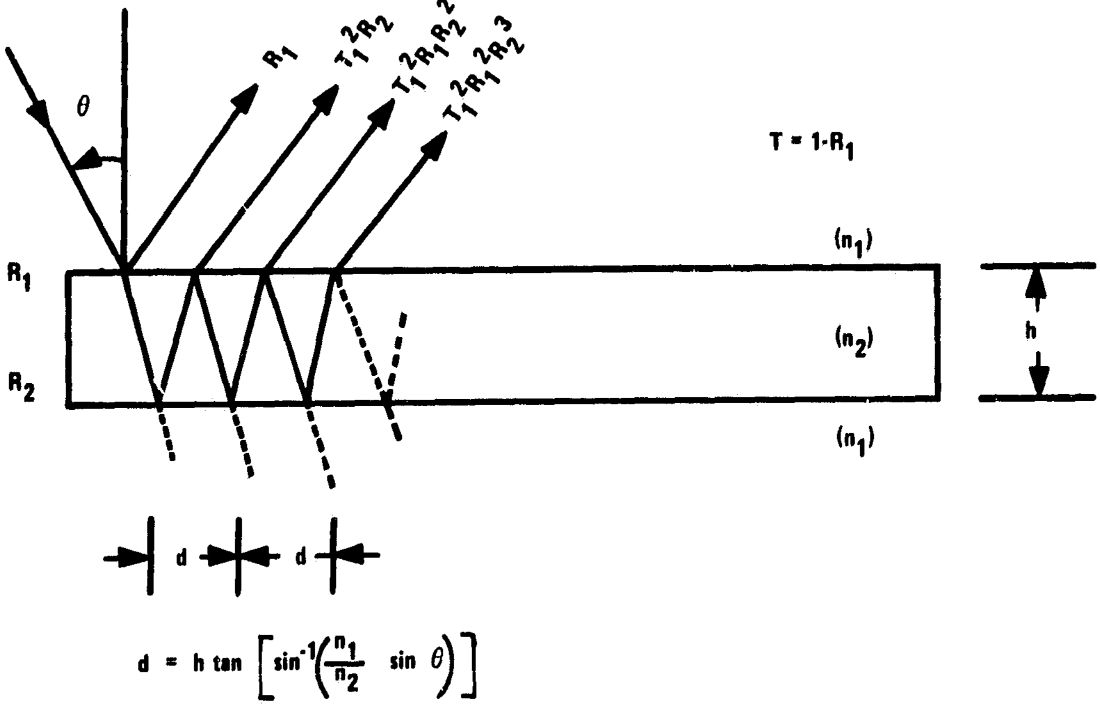

Figure 18. Multiple Surface Reflectance From the Beamsplitter

The equation is totally symmetric in terms of front and back surface reflectances R_1 and R_2; hence, the total reflectance is independent of whether the beam strikes the higher or lower reflectance surface first.

When a reflectance measurement is made with an instrument having a narrow aperture slit, the walk-off of the beam limits the number of reflected rays that can be collected by the aperture. For a double bounce measurement having an 8° incident angle and a 0.1-in. thick substrate, the beam reflected from the back surface is displaced laterally 0.0373 in., the second reflection 0.0745 in., etc. If only the primary reflection and one reflection from the second surface are summed, the reflectance is given by

$$\overline{R} = R_1 + (1 - R_1)^2 R_2 \tag{2}$$

Since the beamsplitter can be oriented with the coated side ($R \approx 0.95$) toward the beam or the uncoated glass ($R = 0.04$) side toward the beam, the net collected energy can be different. In Case 1, coating toward the beam, $R_1 = 0.95$, $R_2 = 0.04$ the net reflectance measured would be $\bar{R}_1 = 0.95010$. In Case 2, $R_1 = 0.04$, $R_2 = 0.95$, the net reflectance is $\bar{R}_2 = 0.91552$. This explains why the average reflectance measured with the glass side toward the spectrometer beam (Figure 17) is 3% to 4% lower than when measured with the coated side toward the beam (Figure 16).

It is suspected that the high frequency modulation of the reflectance that appears in Figure 16 and not in Figure 17 is due to interference between layers within the coating since it stops abruptly at 0.7 µm. The reflective coating appears to contain two discrete reflective stacks, one covering 0.4 to 0.7 µm, the other the 0.7- to 0.9-µm range.

Figures 19, 20, and 21 are the transmission and two reflectances measurements for the 0.70-µm cutoff filter. These curves show characteristics very similar to those of the long-wave cutoff filter previously discussed. In all cases, the transmission portion of the band shows approximately 90% transmission and the reflectance band approximately 95% reflectance.

Multilayer coated filters show an angle of incidence dependence. The filter was designed to operate at a 22.5° angle of incidence, but transmission is customarily measured at normal incidence and reflectance at a fixed angle between 8° and 30°, depending on reflectometer design. To determine the effect of incidence angle on transmission, the sample holder was rotated and transmission measured at 0°, 22.5°, and 30° for each of the beamsplitters. The results are shown in Figures 22 and 23 for the long-wave and short-wave cutoff filters. Increasing the angle of incidence from 0° to 22.5° shifts the cutoff to approximately 0.2 µm shorter wavelength. All other transmission and reflectance features are shifted with no significant changes in total reflectance or transmission.

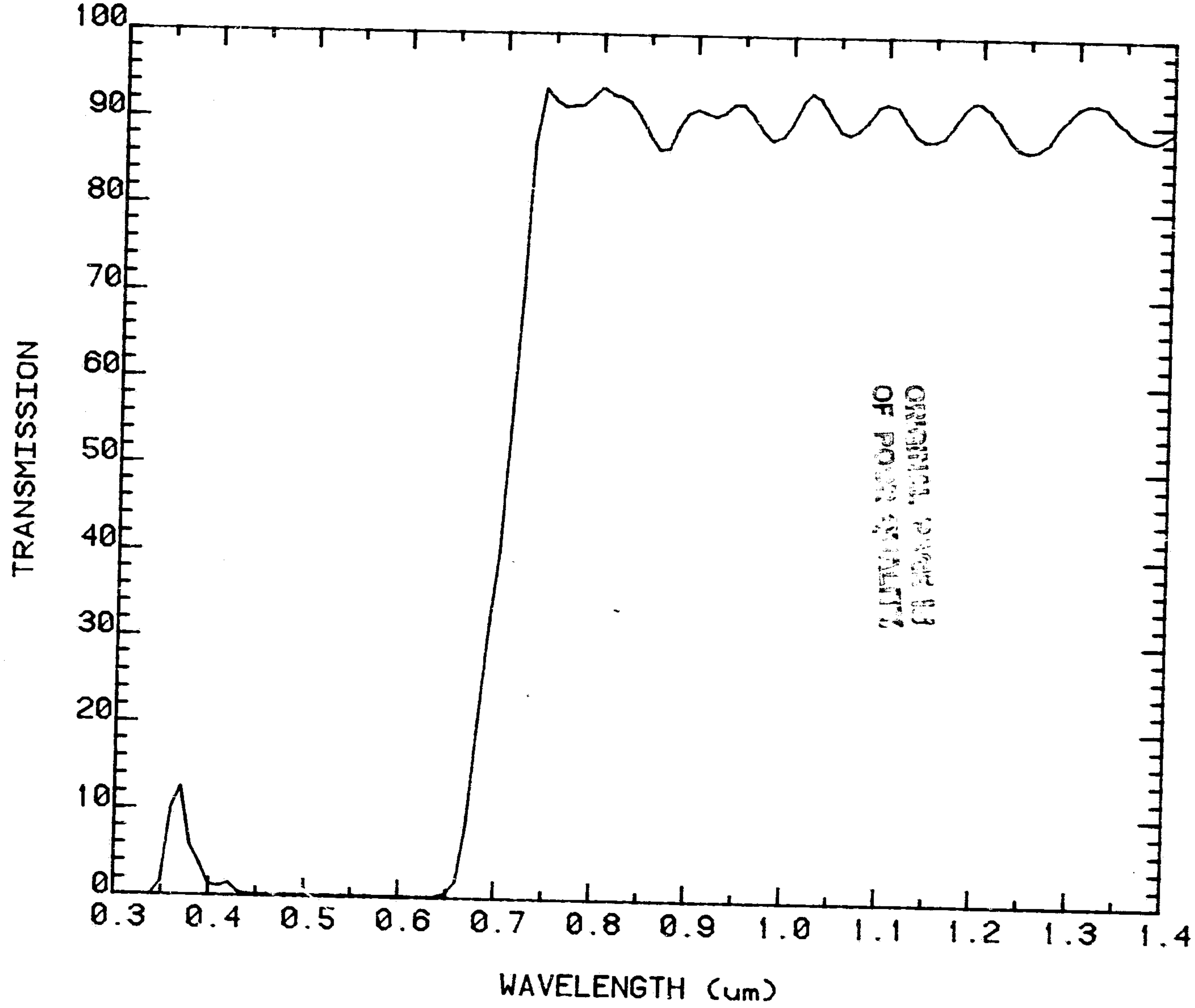

Figure 19. Measured Beamsplitter Transmission (22.5° BS #2)

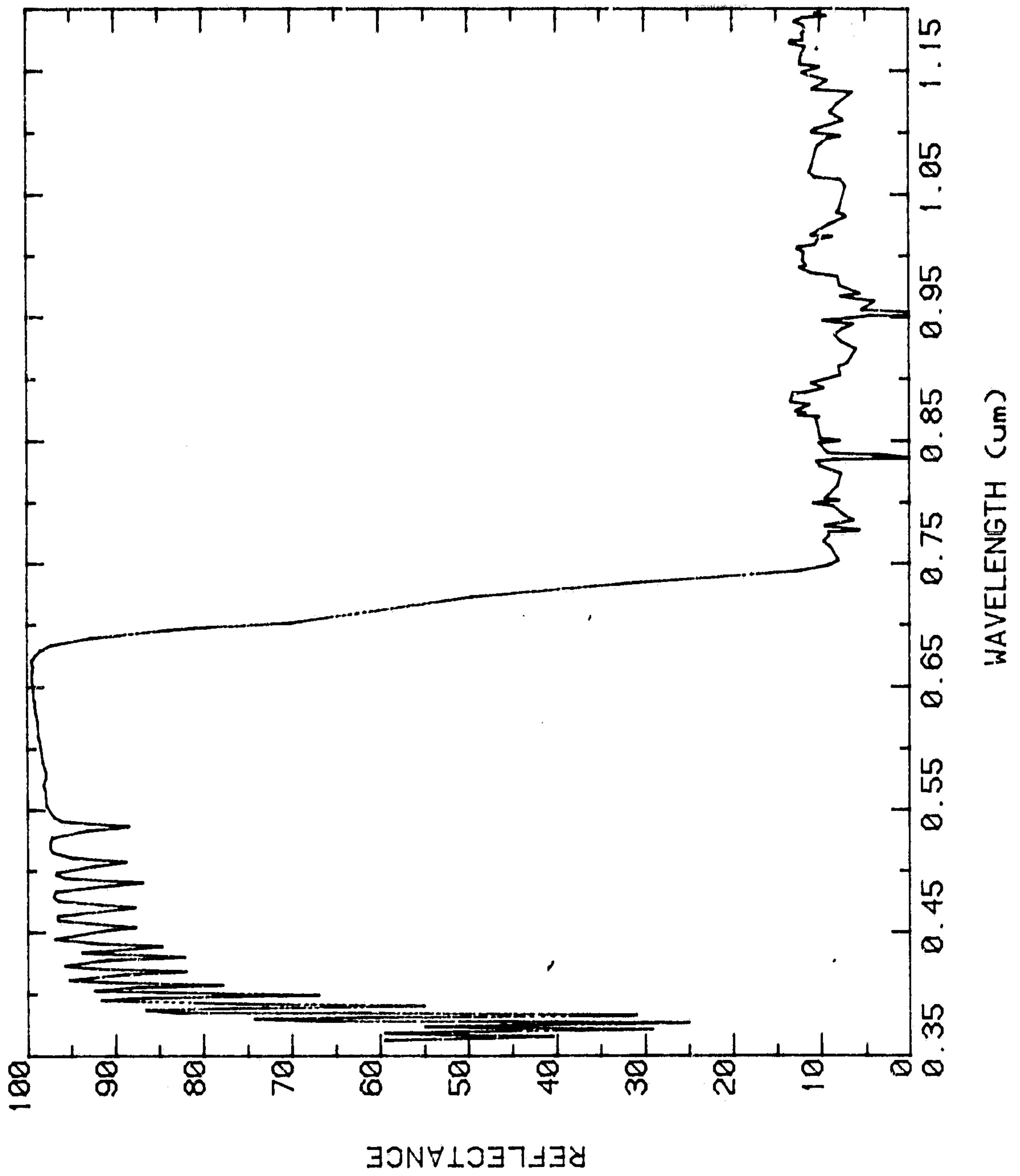

Figure 20. Reflectance, Coating Side Toward Beam (BS #2)

ORIGINAL PAGE IS
OF POOR QUALITY

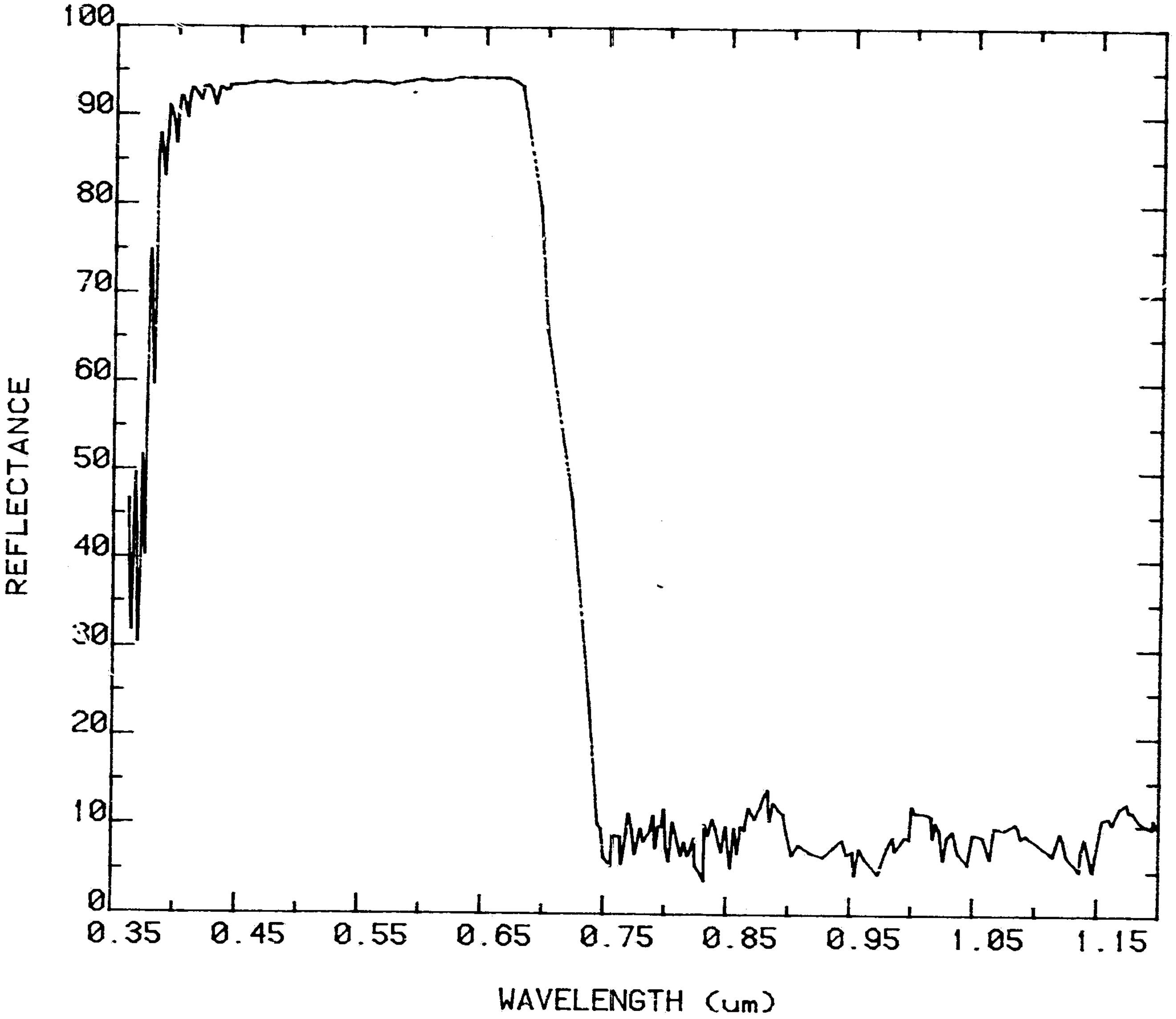

Figure 21. Measured Reflectance, Glass Side Toward Beam (BS #2)

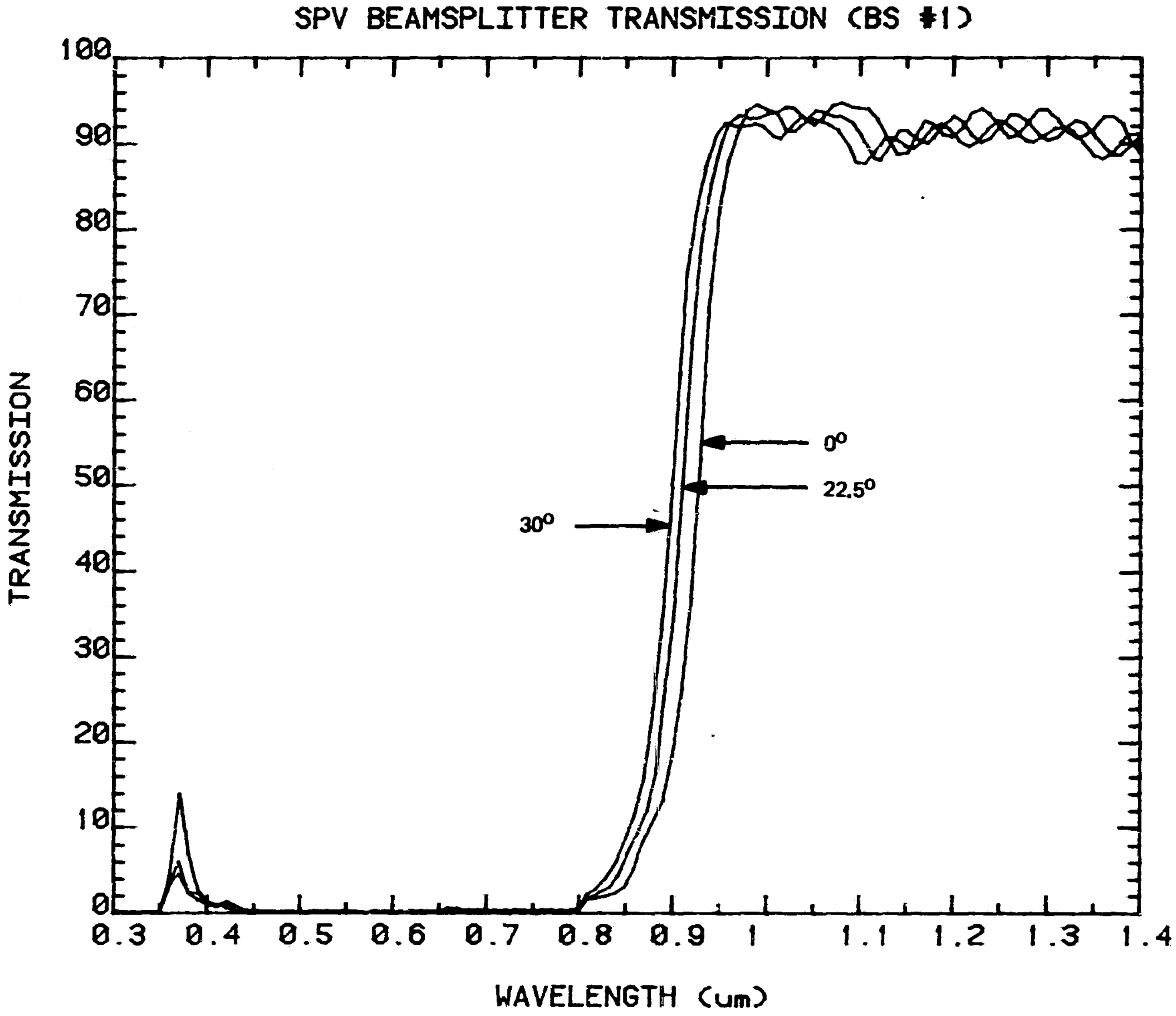

Figure 22. Beamsplitter Transmission as a Function of Incident Angle (BS #1)

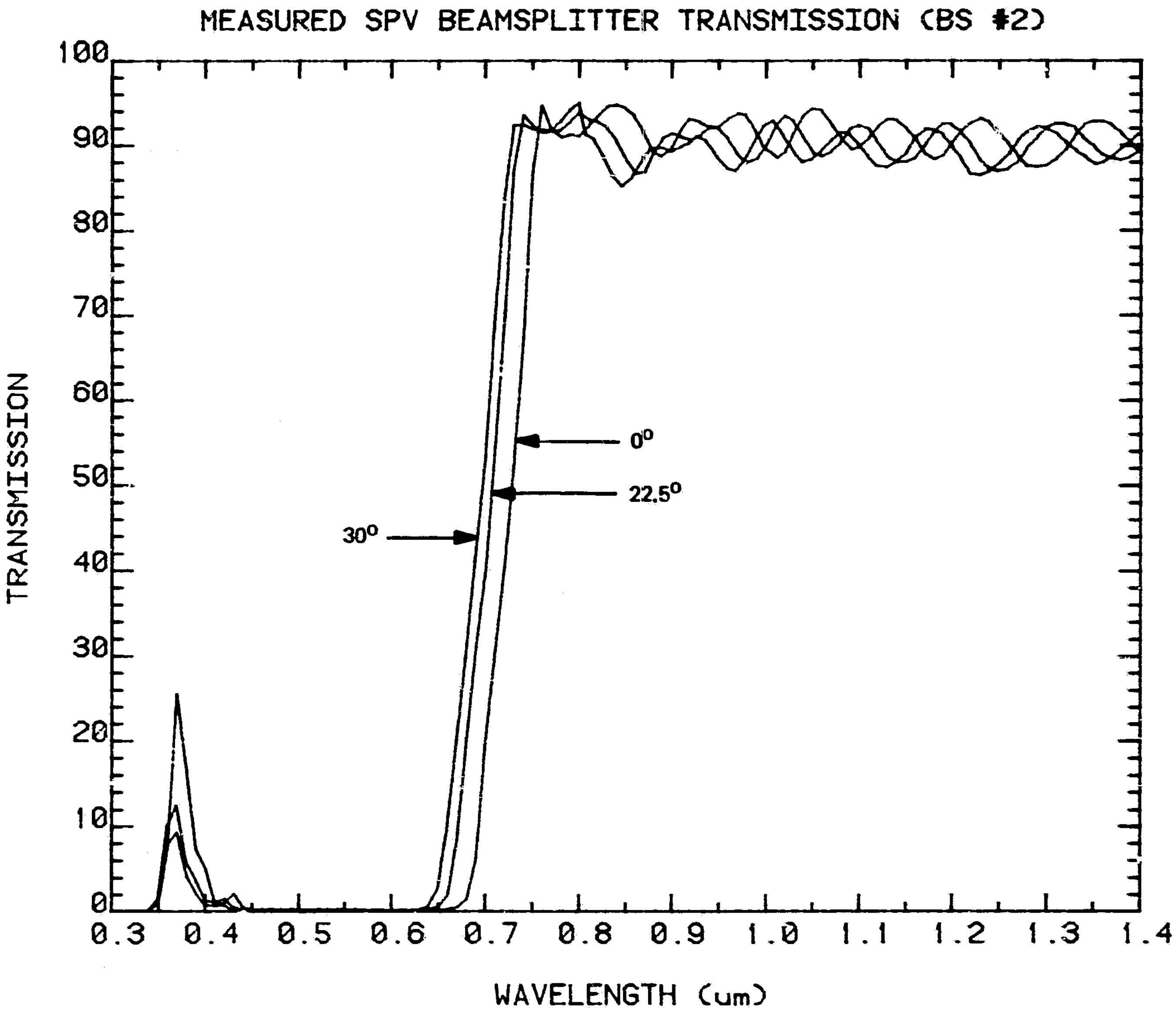

Figure 23. Beamsplitter Transmission as a Function of Incident Angle (BS #2)

Compound Parabolic Concentrators

The compound parabolic concentrators perform the final stage of optical concentration. Using two stages of optical concentration allows the beamsplitter to function in a relatively collimated beam at moderate concentration ratios. Low concentration at the beamsplitter reduces the temperature rise on this passively cooled component. Further, by functioning in a more nearly collimated beam, the beamsplitter cutoff wavelength can be more sharply defined.

The CPC aperture is oversized sufficiently to collect the light from a 1° wide field of view. This permits the system to function with small pointing and tracking errors and compensate for spreading of the beam due to mirror imperfections. The mirrors will have small slope errors and a small amount of beam spreading due to nonspecular reflectance.

Figure 24 is a cross-sectional drawing of the CPC showing the geometry of the electroformed nickel structure. With the solar disk centered, only 38% of the energy strikes the CPC and makes only one bounce before reaching the solar cell. As the tracking error increases, more of the energy is incident on the CPC wall. The angle of incidence ranges from 45° to near 0°. For a perfect tracking system, 38% of the total energy is incident on the CPC walls and the angles of incidence change from 45° to 62° from the normal. The reflectance of polished nickel integrated over the solar spectral range appears to be in the 70% range with no strong angular dependence for the operating range.

The maximum energy loss due to CPC absorption is the product of incident energy times one minus the reflectance (2.38 x (1 - .7)), or 11%. Coating the inside of the CPC with a high-reflectance multilayer coating could improve the reflectance to 95% and cut the CPC losses to near 2%. The small size and poor aspect ratio--i.e., great depth-to-diameter ratio--made this impractical. A

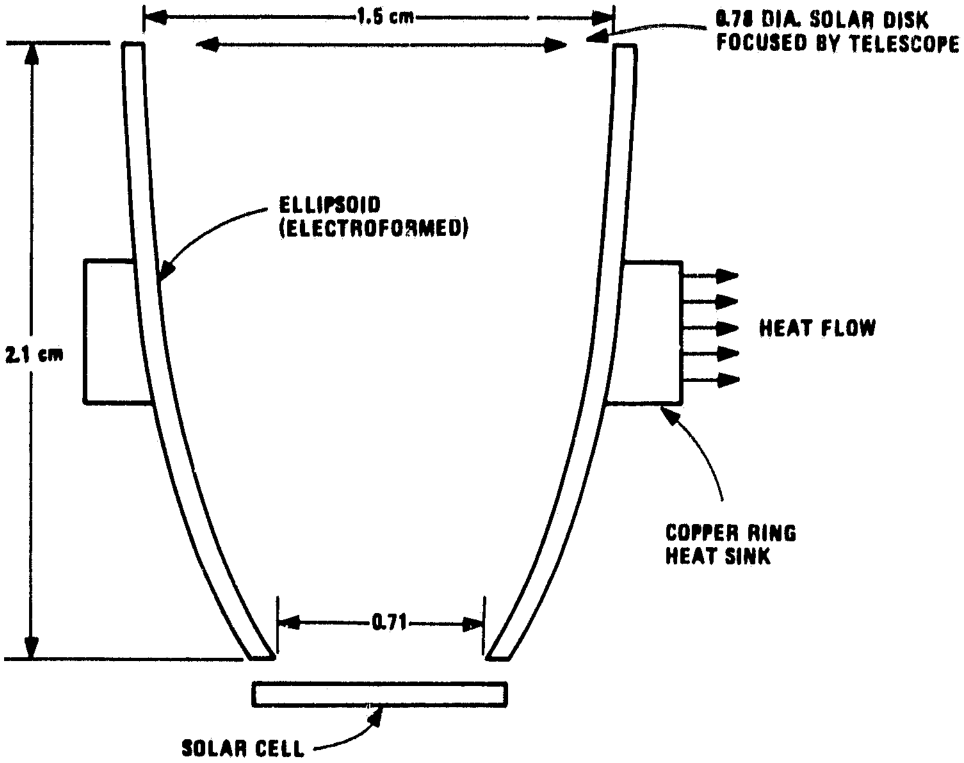

Figure 24. Compound Parabolic Concentrator Cross Section

possible way of increasing coating uniformity would be to cut the CPC lengthwise into three or more sections. These are areas for further evaluation and system improvement.

Solar Cells

The solar cells form the last and most important link in the SPV conversion system. The choice of solar cells was restricted to those that were currently available and that would meet the 1000:1 concentration ratio requirements. Three cell types were available: silicon, gallium arsenide, and aluminum gallium arsenide (AlGaAs). The nominal open-circuit operating voltages of the three cells were 0.7, 1.1, and 1.3 volts, respectively. Varian Associates of Palo Alto, California, was able to provide all three types of cells designed and packaged to operate at 1000:1 solar concentration.

To compare solar cell performance, two common comparisons were used--quantum efficiency and power output. Quantum efficiency is the ratio of electrons collected per incident or absorbed photons. Given cells of the same output voltage, quantum efficiency is a good measure of relative efficiency and is a good diagnostic tool for evaluating cell performance. When comparing solar cells having different output voltages--e.g., Si, GaAs, and AlGaAs--power output is a better measure for comparison. At a given wavelength, the quantum efficiency of an Si cell may be 20% higher than that of an AlGaAs cell, but the output voltage of the Si cell is only 54% of the AlGaAs cell. Hence, at that wavelength, AlGaAs will have a higher power output. For photovoltaic systems employing multiple solar cells of different output voltages, power output is a better basis of comparing cell performance.

Figure 25 is a plot of the quantum efficiency versus wavelength for the three types of cells. The AlGaAs exhibits a lower peak quantum efficiency and a significant fall-off as the wavelength approaches the long wavelength cutoff valve. When these same data are multiplied by the output voltage, the relative areas under the curves change significantly. Figure 26 plots the relative power output determined by multiplying spectral quantrum efficiency by open-circuit voltage. In this plot, the higher output voltage of the AlGaAs and GaAs cells show their importance.

Multiplying the power output by the AMO and AM2 solar spectral energy provides the final basis of comparison of the solar cells (Figures 27 and 28). Because the AlGaAs cell quantum efficiency rolls off too much before the long-wave cutoff, the AlGaAs/Si cell combination power output is less than that contributed by the GaAs/Si cell combination. Thus, of available cells, the GaAs/Si combination was selected for testing.

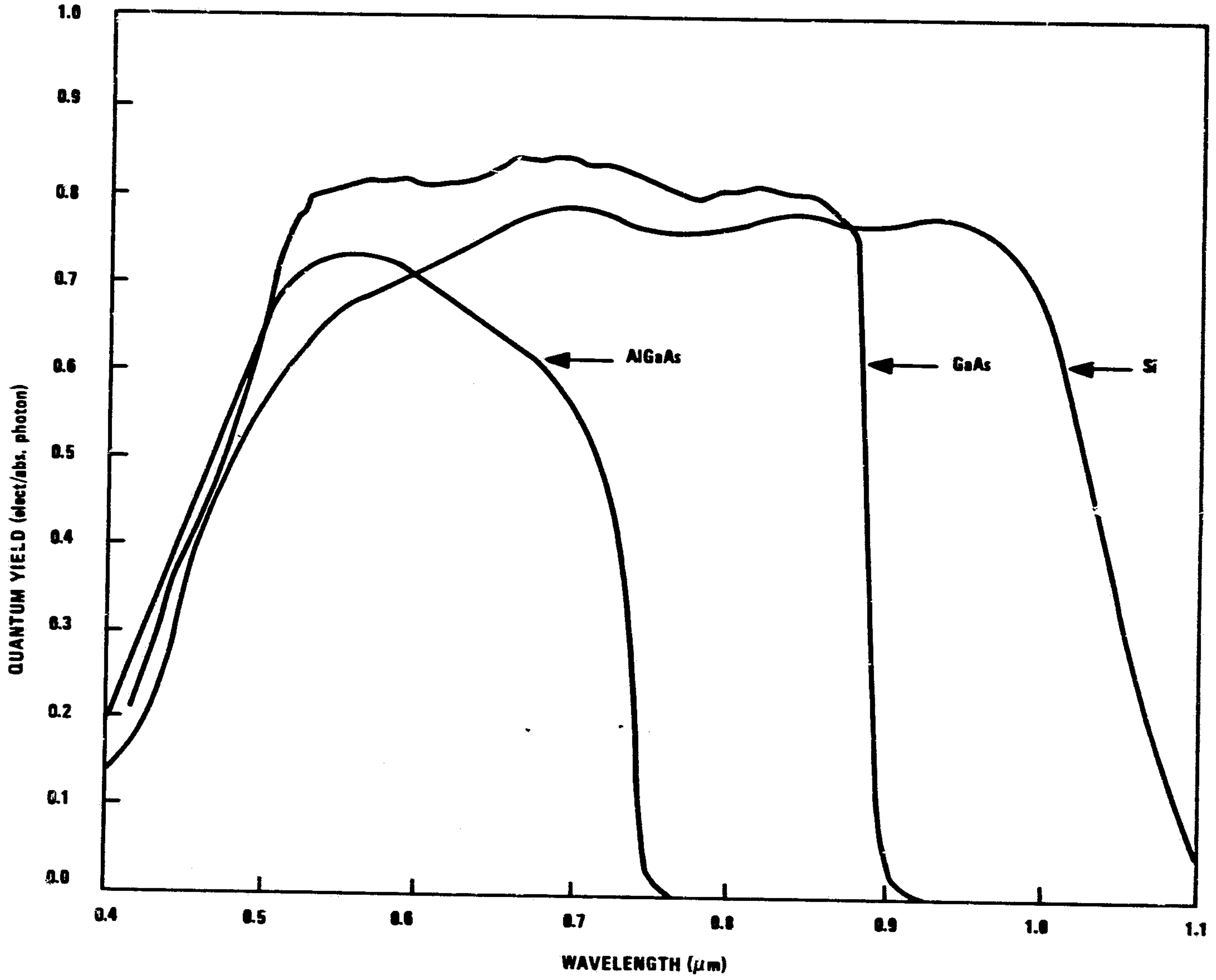

Figure 25. Solar Cell Quantum Efficiency Comparison

ORIGINAL PAGE IS
OF POOR QUALITY

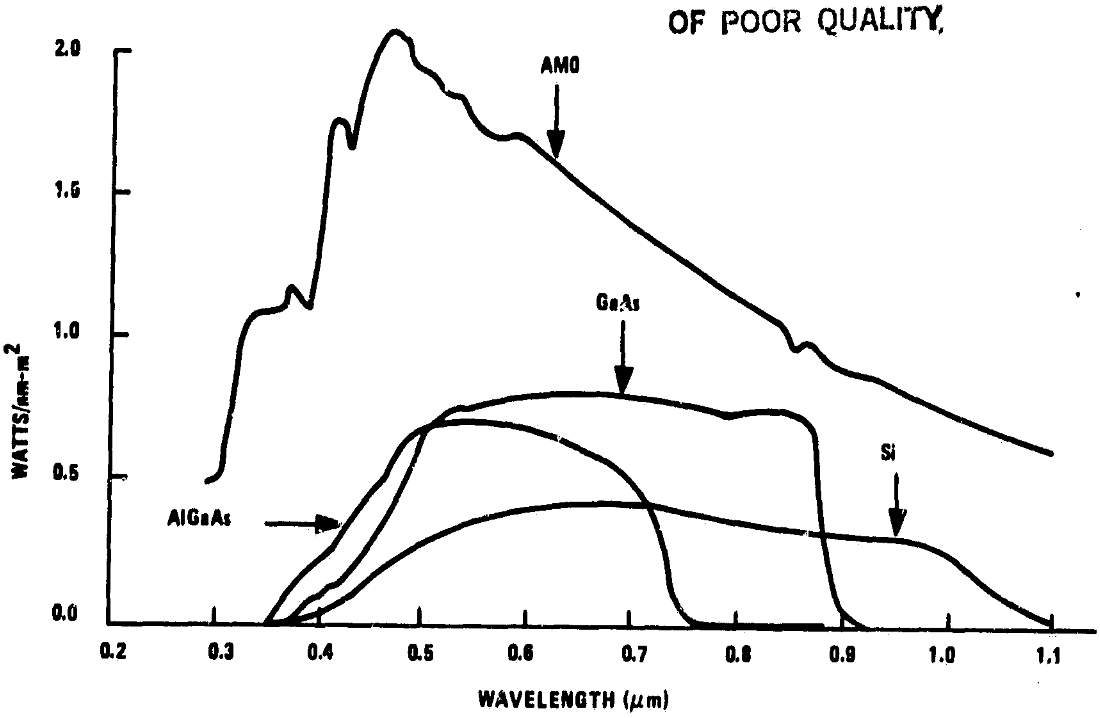

Figure 26. Comparison of Cell Power Output

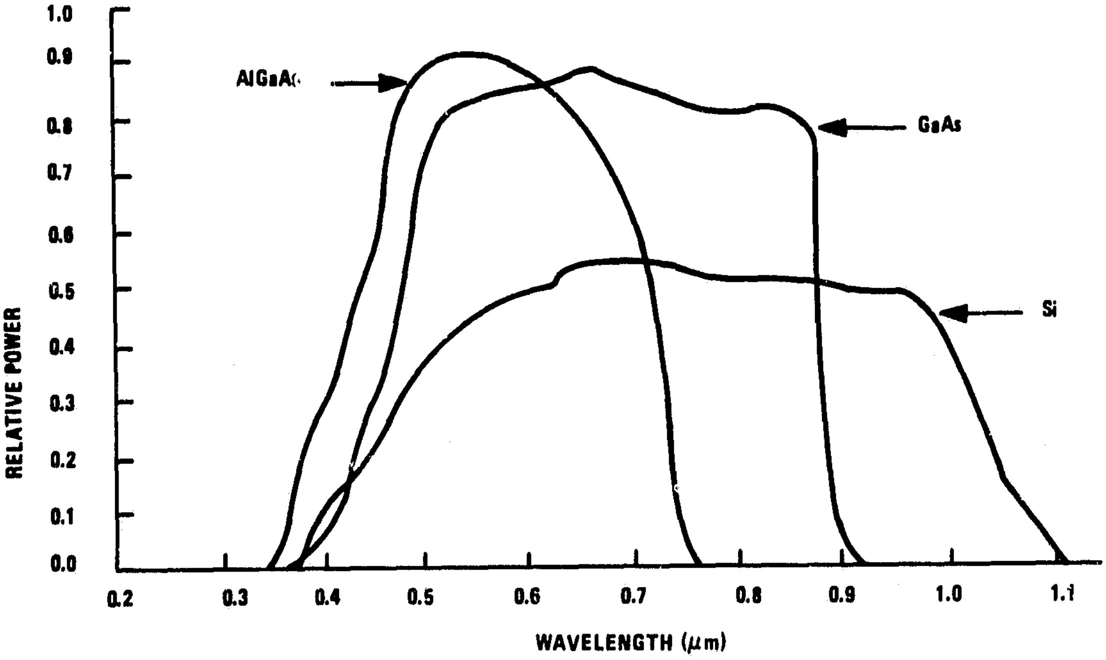

Figure 27. Spectral Power Output for Three Solar Cells at AMO

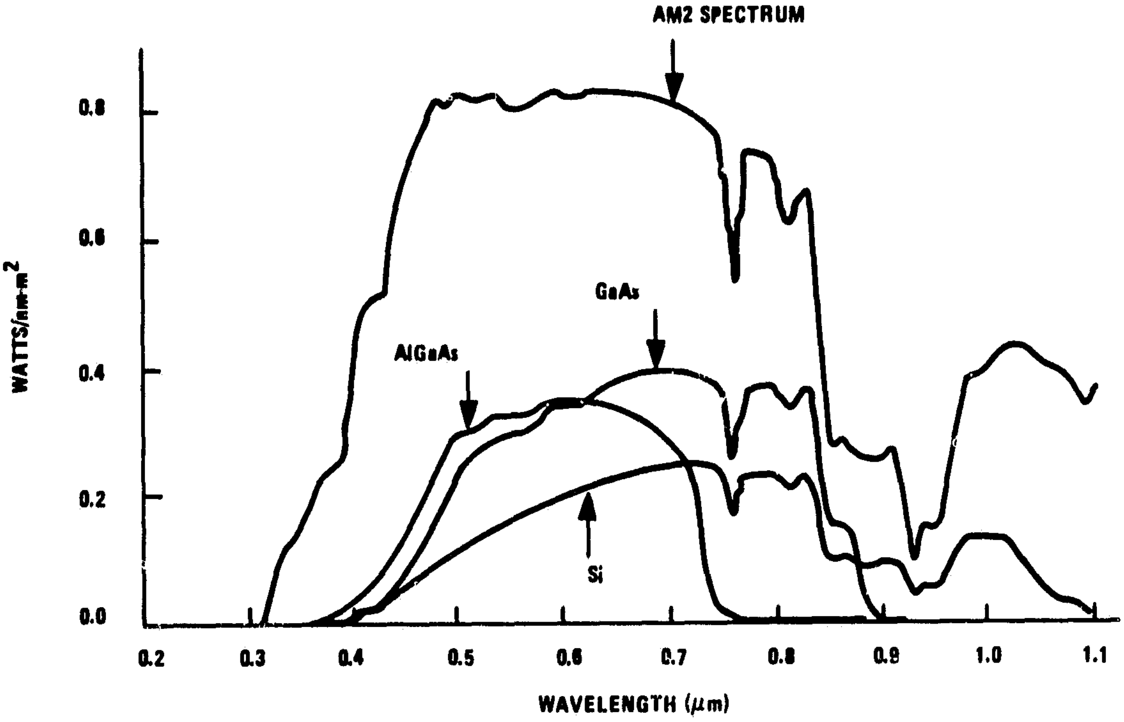

Figure 28. Spectral Power Output for Three Solar Cells at AM2

When comparing individual cells, the Si cells are more efficient than the available AlGaAs cells at all air masses, and the GaAs cells are significantly better than either. When comparing two cell system performance (AlGaAs/Si and GaAs/Si), the differences are not quite as great but are significant and increase with increasing air mass. If the AlGaAs cell quantum efficiency did not roll off so rapidly at long wavelengths, the AlGaAs/Si combination would be better at AMO.

The GaAs solar cell provides significantly greater efficiency by all of the comparison methods. Although it is claimed that better AlGaAs cells are available, there are also slightly better GaAs cells available.

Since the GaAs/Si solar cells exhibited the best performance, this combination was the only combination tested and is reported in Section 4.

SECTION 4

TEST RESULTS AND ANALYSIS

TEST DESCRIPTION

The main objective of the tests was to evaluate the SPV system performance under natural sunlight. Tests were conducted to evaluate system performance, individual cell performance, field of view, thermal response, and instrumentation.

Most of the theoretical calculations were based on clear sky AM2 spectrum or an AMO spectrum. Because of the low solar-declination angle during the late November test period, most of the tests were conducted between AM2 and AM3. The high air mass tends to shift the solar spectrum toward longer wavelengths, with a resulting decrease in overall system efficiency. This will be discussed further when comparing the calculated and measured system output.

The tests were conducted on the Honeywell Systems and Research Center roof top which provided on unobstructed solar view, access to electric power and heat, and restricted personnel access. The geographic coordinates of the test site were 45°OON, 93°13'W with an elevation of approximately 850 feet above mean sea level. The longitude was such that solar time was within two minutes of central standard time (CST); hence, data reported for CST are essentially corrected for apparent solar time.

The procedure used to obtain the current-voltage (I-V) curves for the solar cells was to align the concentrator to the sun to maximize the short-circuit current output and then vary the series resistance from 0 Ω to ∞ (short circuit to open circuit) in steps from which the complete I-V curve could be plotted. Due to a small mechanical misalignment of one of the solar cells, measurements for each cell exhibited maximum power output at a slightly different alignment. Hence, the I-V curves for the two cells were measured sequentially rather than simultaneously.

Figure 29 shows the system in its test configuration on the roof top. The picture shows the SPV concentrator on an Epply equitorial drive unit with the variable resistance box and cooling water system placed on the lower shelves of the laboratory cart. The data logger, not shown, was located indoors. Tests were conducted on November 16 and 18, 1982, during the morning hours. Near noon on each day high cirrus clouds moved in and prevented further testing.

TEST RESULTS

The test results presented in this section are the I-V curves for each solar cell, the I-V curve for the silicon cell without the beamsplitter, the system thermal response, and the field-of-view tests. Each of the test results is presented graphically, with a discussion of the results and test conditions. Comparisons between the measured results and the modeling predictions will be made in the following section.

Figure 30 is a plot of the I-V curve for GaAs cell operating with the beamsplitter reflecting light onto it. The data were taken over a period of 18 minutes during which the solar intensity varied ±1.3%. The maximum power point was determined by fitting a curve through the measured data and differentiating to determine the maximum power point. The cell efficiency of 12.68% was determined by dividing the maximum power output by the effective power input. The power input was taken as the product of net collector area, primary mirror area minus secondary mirror obscuration,* and solar flux measured with the calibrated pyrheliometer.

The long wavelength energy, 0.9 to 1.1 μm in wavelength, was transmitted through the beamsplitter to the Si cell. The Si cell I-V curve is plotted in Figure 31. The voltage scales in Figures 30 and 31 are similar, but the

---

*Secondary mirror obstruction was 10.1% of the aperture area.

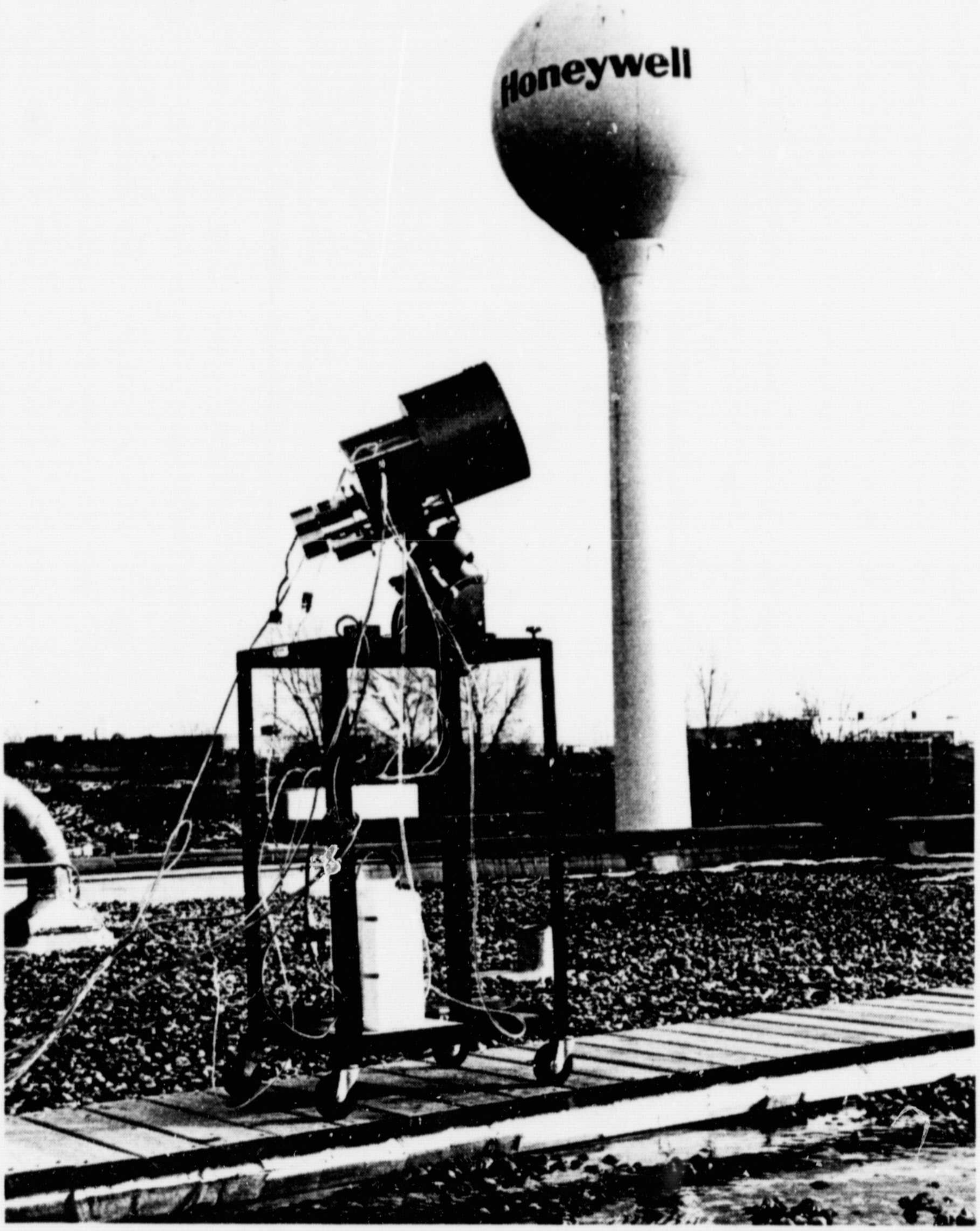

Figure 29. SPV System Test Configuration

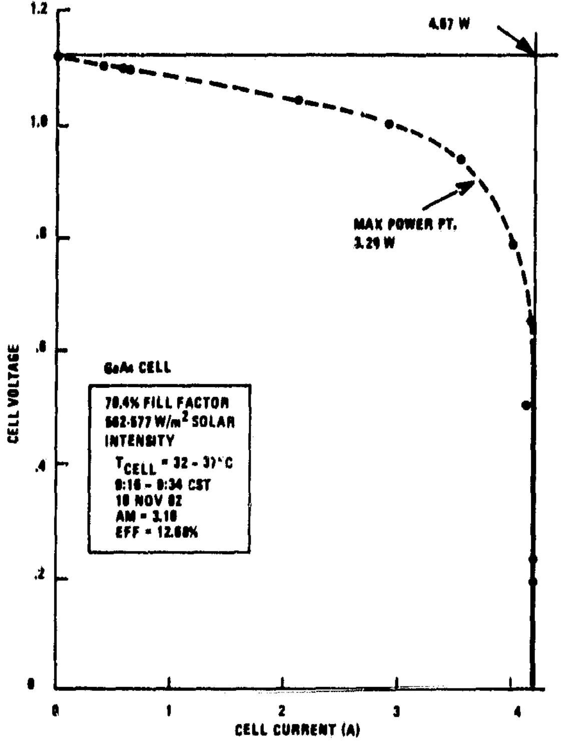

Figure 30. Gallium Arsenide I-V Curve

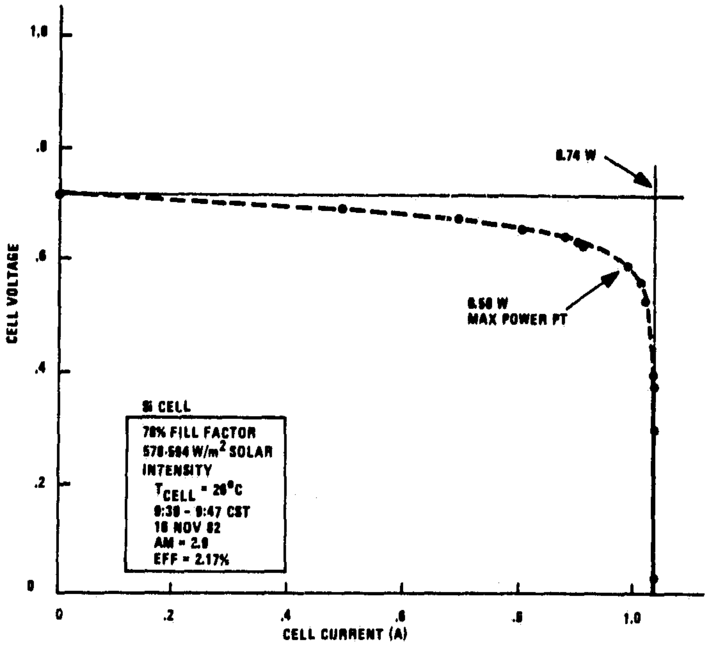

Figure 31. Silicon Cell I-V Curve

current scale was changed to provide a reasonably proportioned graph. Since 64% of the AM2 solar energy occurs at wavelengths less than 0.9 μm, a large difference in current output can be anticipated. The Si cell fill factor is higher than that of the GaAs cell because the cell is operating at a current considerably below its maximum current design point.

When the power output of the GaAs and Si cells (Figures 30 and 31) are combined, the system efficiency was 14.85%. This efficiency is considerably less than the 20% anticipated earlier in the program. The major causes of the poor performance are the low reflectance values for the two mirrors and the CPCs, with a minor contribution due to absorption in the beamsplitter. The effects of the components will be discussed further in the modeling discussion.

The I-V curves were generated a second time on November 18. Although the experiments were run later in the morning when the sun was higher and the intervening air mass lower, the sky was hazier. The result showed up as a slightly lower solar flux. The I-V curves measured on November 18 for the GaAs and Si cells are presented in Figures 32 and 33. The efficiency of the GaAs solar cell appears to be slightly higher--13.38% versus 12.68%. The differences between the two test results appear to be related to the solar flux levels. As the solar flux decreases, the cell current decreases and the internal resistive losses in the cell decrease. The result is that the fill factor increases. If, in the case where the spectral distribution of energy is approximately the same, the cell efficiency increases. The slope of the GaAs I-V curve from 0 to 3 A indicates that the cell and its mount had an internal resistance of approximately 0.0353 Ω. Assuming an initial condition of an open circuit voltage of 1.13 V, the fill factor would decrease by 3.5% per ampere of current draw. Within experimental error, this is the change exhibited between the two test runs (Figures 30 and 32).

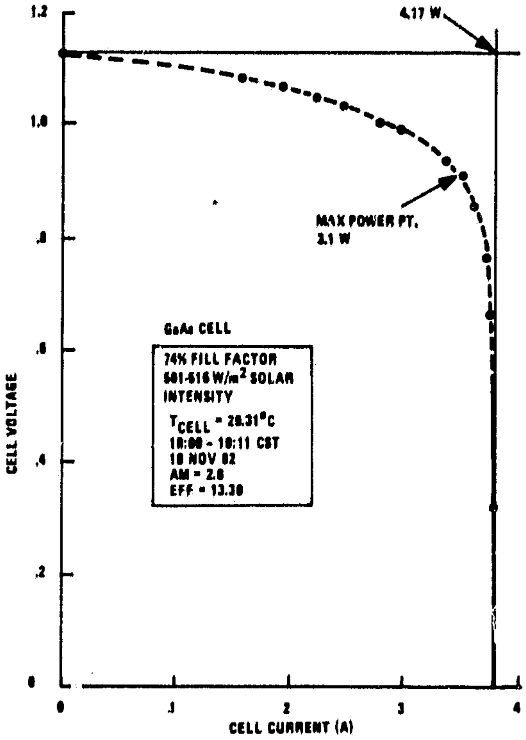

Figure 32. GaAs Cell I-V Curve

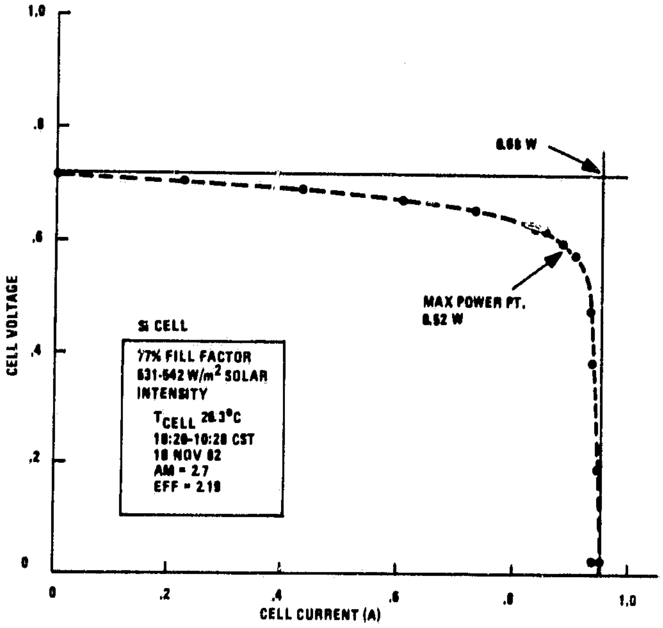

Figure 33. Si Cell I-V Curve

The fill factors for the silicon cells for the two test days were nearly the same--78% and 77%. Since the change in current on the Si cell was a factor of 4 smaller than for the GaAs cell, the effect on fill factor was also reduced. In fact, the internal resistance of the Si cell circuit was also lower--0.0317 Ω versus 0.0353 Ω for the GaAs cell.

Figure 34 presents the I-V curve measured for the silicon cell with the beamsplitter removed from the system. The solar spectrum was concentrated on the single cell. The cell current increased by nearly a factor of 4, the efficiency increased by approximately 3.6, and the fill factor decreased from 77% to 70.9%. The fill factor change is very close to the decrease predicted by the voltage drop due to cell resistance.

With the full solar spectrum concentrated on the solar cell's 0.71-cm diameter, the incident flux was 23.7 W or 59.7 W/cm^2 (0.597 x 10^6 W/m^2).

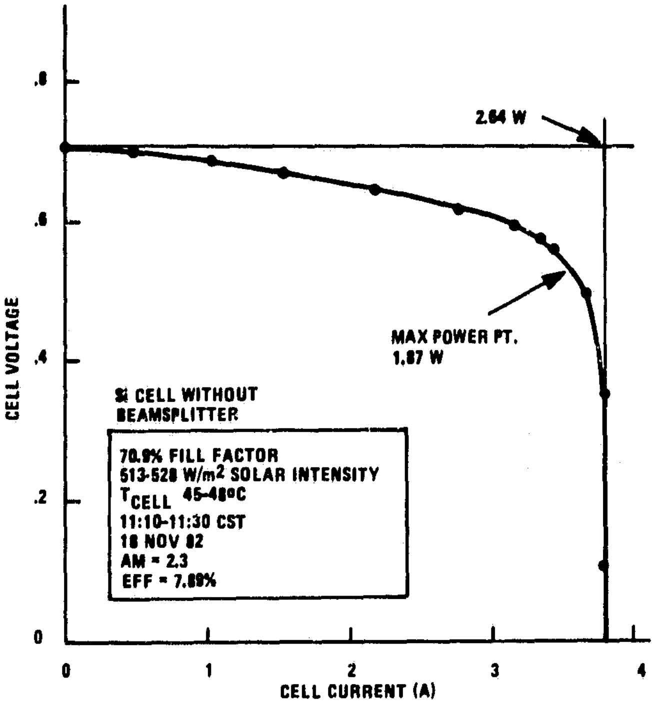

Figure 34. Silicon Cell Tested Without the Beamsplitter

(The heat flux from the cell was not recorded during this test.) The cell temperature was proportionately higher than that of the GaAs cell, indicating that the cooling and temperature measurement systems were operating normally. The increase in cell temperature causes a decrease in output voltage. Data from Reference 2 indicate that silicon cell voltage will decrease at approximately 0.002 V/°C near ambient temperature while the current at the maximum power shows little change. The 20° rise in cell temperature could account for a 0.04-V decrease in cell voltage or approximately 0.53% in efficiency. Cooling the silicon cell to 26°C, as in Figures 31 and 33, would have raised the cell efficiency determined from the data in Figure 34 to 8.42%.

To estimate the field of view of the system, short-circuit cell current was recorded as the sun image moved out of the field of view. Note that short-circuit current is proportional to photon flux while open-circuit voltage is nearly independent of flux. Hence short-circuit current is better suited for detecting tracking errors. Figure 35 shows a plot of solar-cell short-circuit current as a function of time with the right ascension (RA) drive stopped. The sun's apparent position changes at a rate of 1° every four minutes. The design field of view was 1°. When a 0.5° sun is viewed, all of the sun's energy should be collected with a ±0.25° tracking error. Further, all energy should be rejected with a tracking error greater than 0.75°.

There was some difference in the way the two cell currents fell off with time. As observed earlier in testing, there was a small amount of misalignment between the two solar cells. In this test the Si cell was most accurately aligned to the sun, with the result that the GaAs exhibited a small decrease in output from the start of the test. The Si cell output remained relatively level for the first 0.25° (GaAs 91% of max and Si 97% of max), then started to decrease. At 0.5° both cells had an output that was 72% of the maximum; this then dropped off rapidly with a further increase in tracking error.

ORIGINAL PAGE IS
OF POOR QUALITY

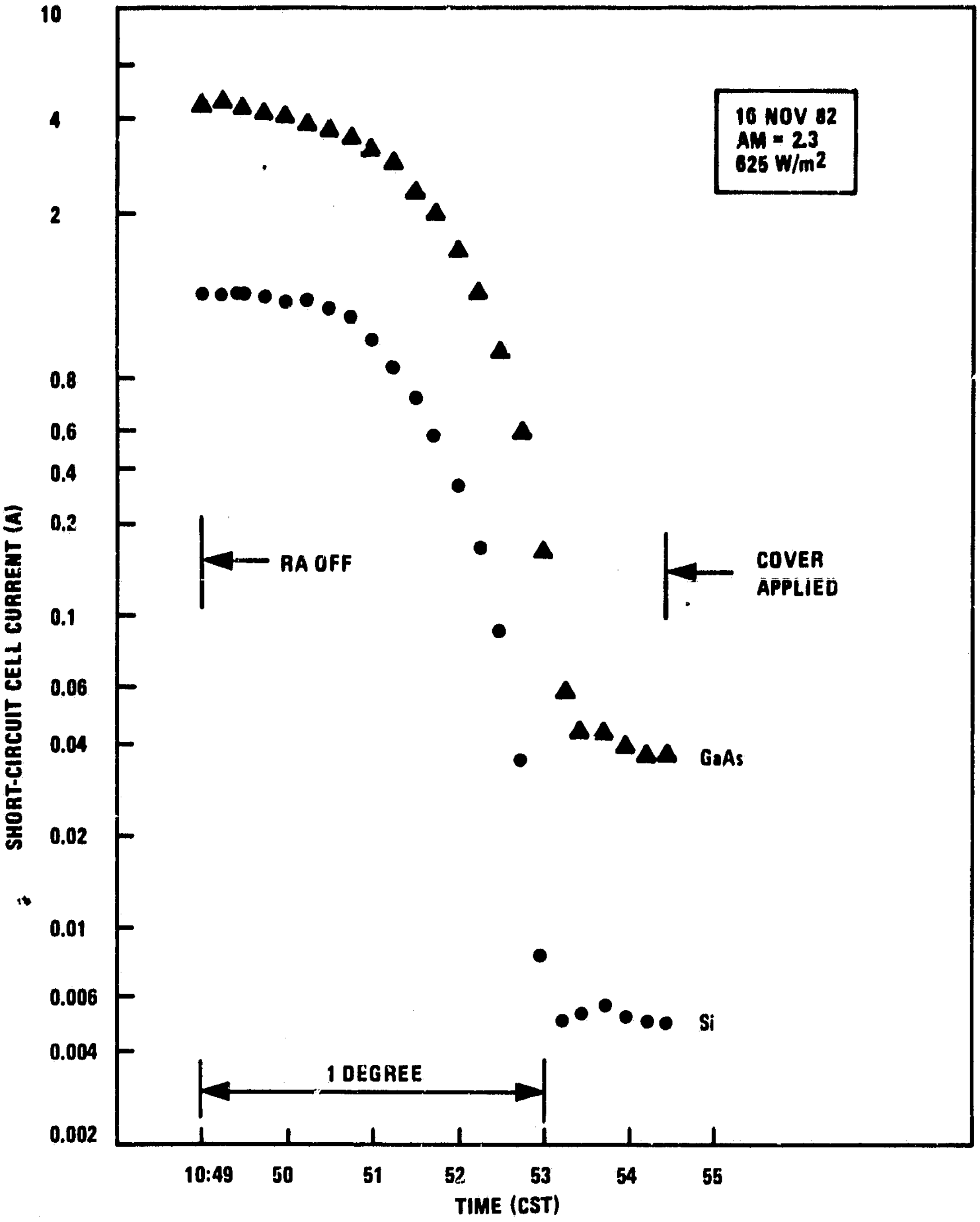

Figure 35. Concentrator Field-of-View Measurement

After three minutes, when all of the theoretical sun's image was falling outside the CPC, the cell current had dropped to 34% on the GaAs cell and 25% for the Si cell. The cell current did not reach 1% of the initial value until the sun image was 1.1° from centered. This could be attributed to a high sky brightness and nonspecular reflectance from the mirror. During the test the sky exhibited some haze due to high-altitude cirrus. The test was discontinued after 5.5 minutes due to excessive heating of the CPC/solar cell holder modules as the sun's image moved across them. The results of this test demonstrated that the CPCs provide a fairly uniform illumination of the solar cell over nearly a 1° field of view.

While the solar cell current as a function of tracking error was being measured, the system thermal response was also recorded. The results for the GaAs cell module are plotted in Figure 36. The module diagram in the upper right corner of Figure 36 indicates the location of the thermocouples. Thermocouples 13 and 14 can be used to estimate heat flux from the GaAs solar cell. The calculated thermal conductance between thermocouples 13 and 14 was 1.17 W/°C. While the cell temperature monotonically declined as the sun's image moved off from the center of the CPC, the CPC temperature increased. During the first minute when the image moved within the CPC, its temperature change was small. The aperture of the cell holder module was larger than the CPC aperture, thus allowing energy to be absorbed directly by the CPC support ring as the sun's image moved outside the CPC. As the sun's image moved outside the CPC, the CPC temperature rose rapidly and then fell sharply as the image moved out onto the face of the aluminum module at about 3.5 minutes into the test.

The temperature of the solar cell and the apparent heat flux from it fell off significantly more slowly than the solar flux. This was due to a considerable mass of copper used in the cell holder and a lower than expected thermal conductance between the cell holder and the water-cooled support. In fact,

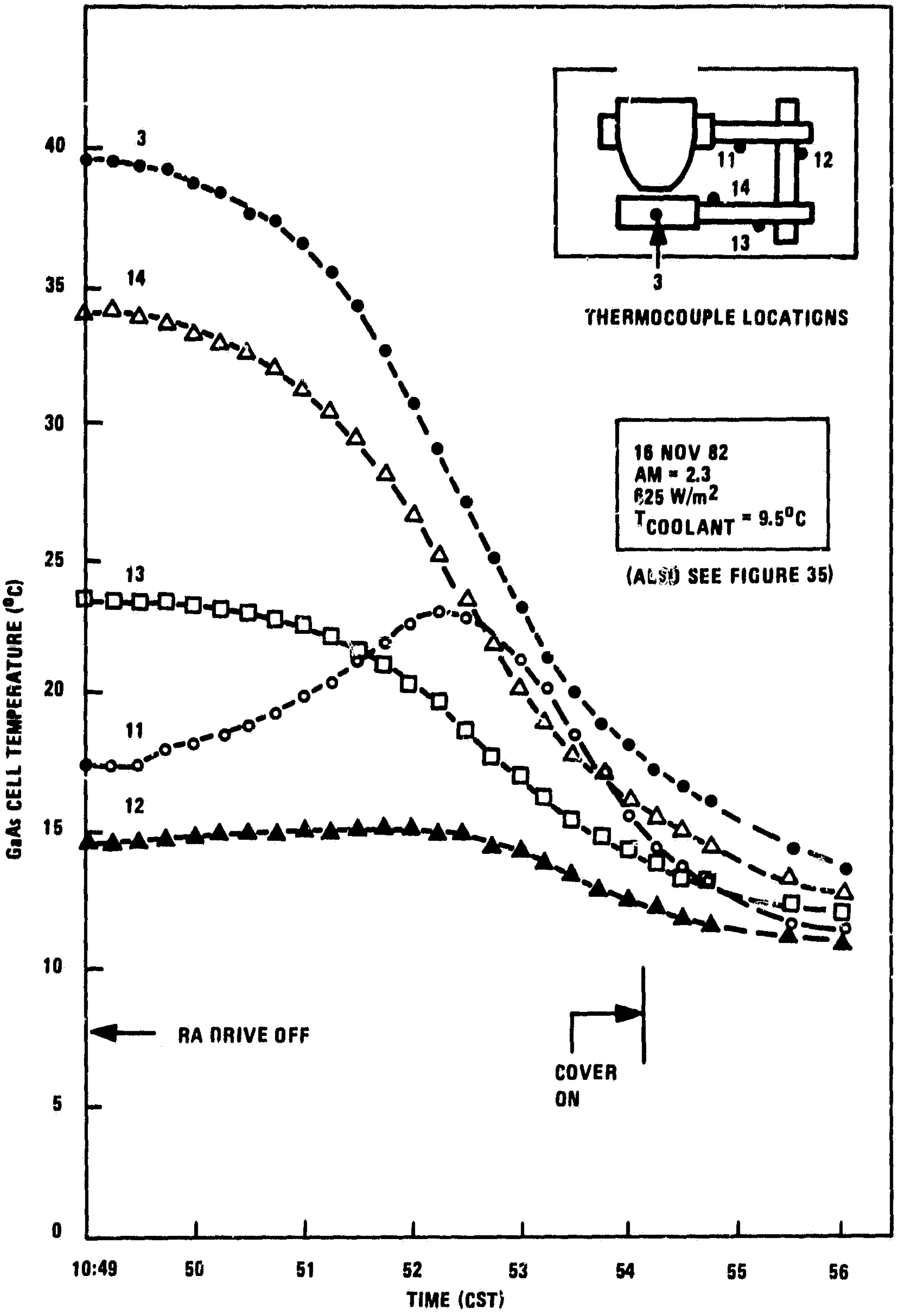

Figure 36. Thermal Response of the GaAs Cell as the Sun's Image Moves Off From the Cell

after the cover was placed on the system, the CPC and holder quickly cooled to a temperature below that of the solar cell. The total heat load into the module indicated by the sink temperature, thermocouple 12, rose slightly as the sun's image moved across the CPC and then dropped rapidly as the CPC temperature fell.

As the field of view of the concentrator was evaluated, the field of view of the pyrheliometers was also checked. Figure 37 plots the output of the two pyrheliometers as a function of time with the right ascension drive turned off. No significant change in signal level was observed until approximately seven minutes had elapsed or the sun had drifted 2° off center. The quoted field of view of the Epply pyrheliometer is 5°43' but that is the field of view at the half-power point. The calculated field of view with no signal blockage is 3°31'. Hence the output signal plotted in Figure 37 should be expected to start falling off after six minutes, reaching the half-power point after 11.4 minutes. The signal started falling off approximately a minute late (0.25°) and appeared to be approaching the half-power point at 11 minutes. The approaching clouds obscurred the exact time. Other than a possible misalignment of the pyrheliometer to the concentrator of ±0.25°, the pyrheliometer was functioning as predicted.

To characterize the solar spectrum, three filters were mounted on the pyrheliometer filter wheel. Knowing the spectral transmission of the filters allows an estimation of the relative amounts of energy reaching each detector. The three Schott Glass filters on OG-530, on RG-695, and RG-780 were used. Their measured spectral characteristics are shown in Figure 38. The measured cut-on wavelengths were 530 μm, 695 μm, and 800 μm, with 90% transmission out to 2 μm and then a sharp cutoff at 2.7 μm. Table 2 lists the measured solar flux using each of the filters and compares it to the

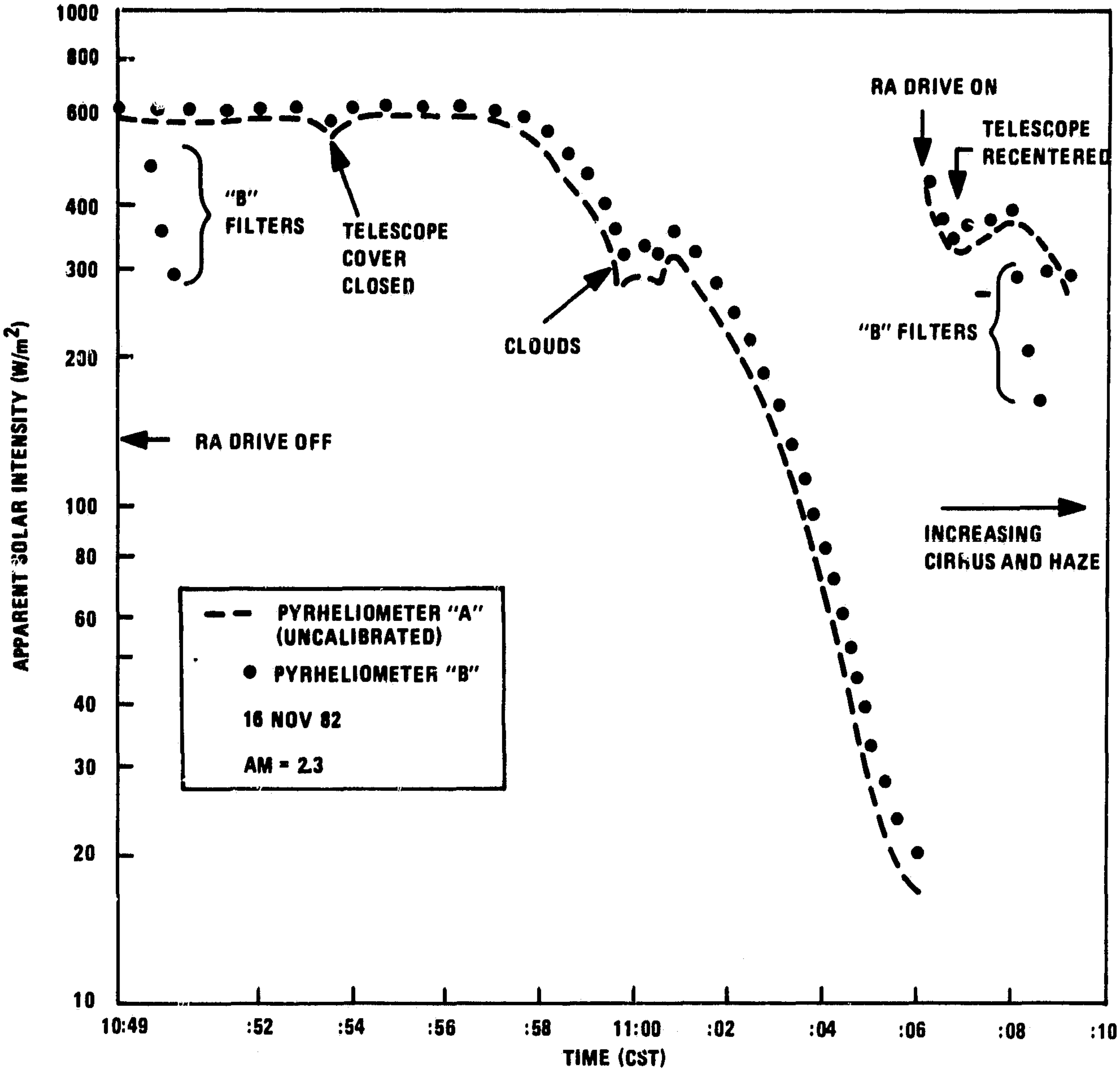

Figure 37. Pyrheliometer Field-of-View Verification

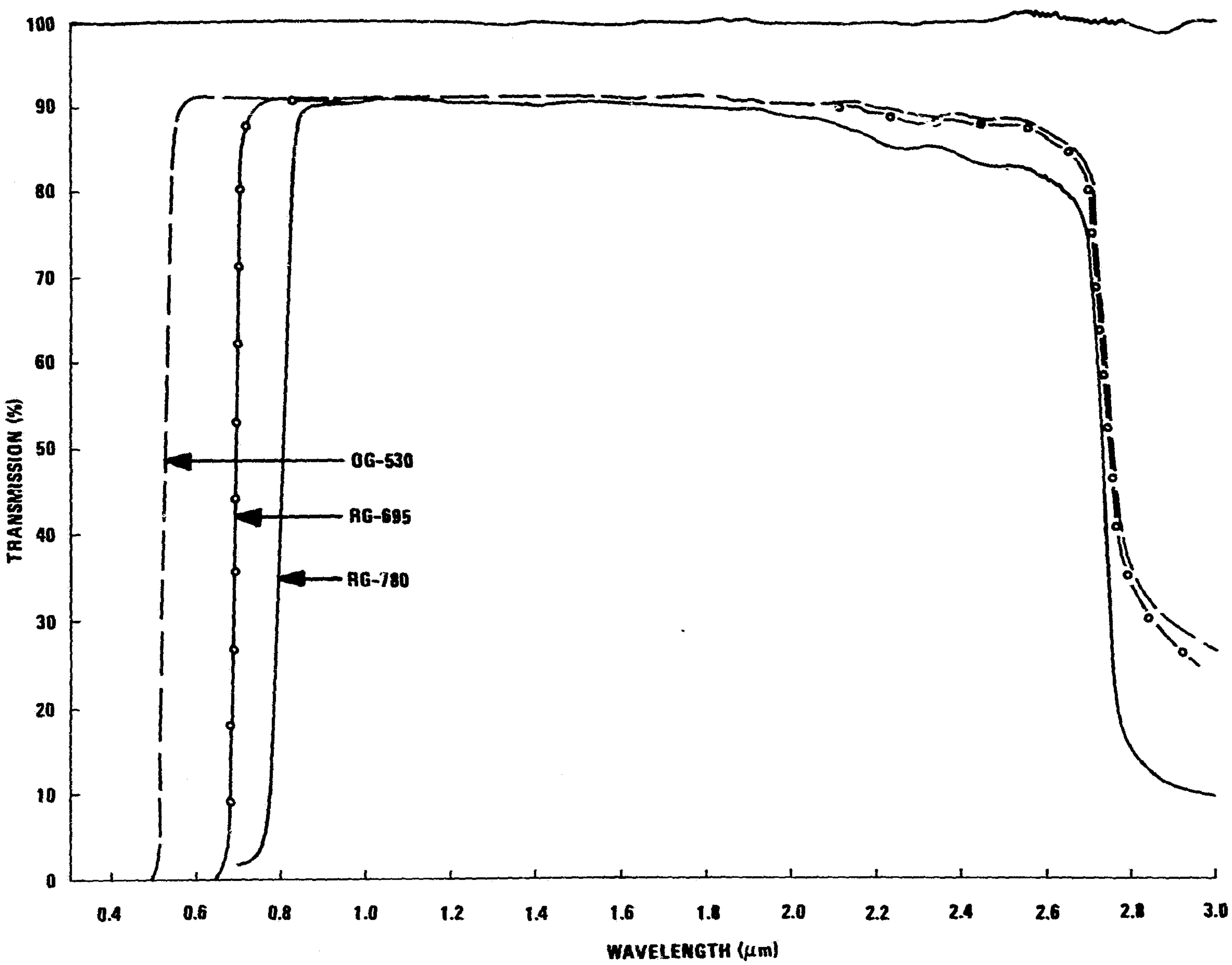

Figure 38. Pyrheliometer Filter Characteristics

TABLE 2. MEASURED SPECTRAL FLUX DISTRIBUTION

	Filter	Spectral Range (μm)	Trans-Mission %	Calcu-lated Flux (W/m^2)	Measured Flux (W/m^2)	Scaled Calcu-lated Flux	Measured Differ-ence (%)
AM2 (Calculated)	None	0.3 to 4.0	100	563	---	623	--- + 10.7
Pyrheliometer (Measured)	None	0.3 to ≃4.0	100	563	623	623	0.0
	OG-530	0.53 to 2.7	.90	403	484	446	+ 8.5
	RG-695	0.695 to 2.7	.90	281	363	311	+ 16.7
	RG-780	0.80 to 2.7	.90	223	295	246	+ 19.9

expected flux assuming an AM2 atmosphere and turbidity coefficients of α = 0.66 and β = 0.17. Although the calculated air mass was 2.3, the measured intensity was 10.7% greater than the theoretical value for AM2. This can easily be accounted for by observing that if the turbidity coefficient β is cut in half, the AM2 flux increases from 563 to 691 W/m^2. Interpolating between AM2, AM3, and turbidity coefficient β = 0.085, and β = 0.17[1] indicates measured flux of 623 would require a turbidity coefficient of β = 0.10, which is representative of moderately clear air. The spectral shift toward longer wavelengths due to increased air mass only accounts for about two to three percentage points. The remainder of the measured spectral shift remains unexplained. In the final analysis, none of the spectral shifts or measured intensities has a strong effect on earlier system efficiency calculations. At the worst, the effect could be on the order of a fraction of a percentage point.

A final look at the thermal response of the solar cells is presented in Figure 39. The temperature rise of the GaAs cell is plotted as a function of time after exposure to the concentrated sunlight. In a period of 37 seconds the temperature rose to 50% of its final value. The initial temperature rise rate was approximately 17°C per minute. In the initial stages of heating, most of the heat goes into the heat of the cell and holder. As the temperature rises further, a gradient is established between the cell and the holder, and heat begins to flow into the water-cooled heat sink. The cell temperature continues to rise until thermal equilibrium is established and all heat is being conducted to the heat sink. The slow establishment of equilibrium--i.e., the last 5° temperature rise requiring 10 minutes--supports the earlier observation that on cooling (Figure 36), the slow decay in cell temperature when the sun moves off from the cell was due to removal of heat and not to a slow decrease in solar flux on the cell.

COMPARISON OF CALCULATED AND MEASURED SYSTEM OUTPUT

In this section the system analytic model will be described, the calculated power output for various operating conditions presented, and a comparison made between measured and calculated conversion efficiencies.

The solar spectral intensity profile for various air masses is plotted in Figure 40. It shows the rapid decrease in solar energy with increasing air mass, the shift toward longer wavelengths, and the strong effect of absorption in the 0.8- to 1.0-μm band. Considering the GaAs and Si solar cell combination, one sees that the relative area under the AM2 curve between 0.3 and 0.9 is much larger than the area between 0.9 and 1.1 μm. Further considering that the GaAs output voltage is 57% higher, 1.1 V versus 0.7 V, it

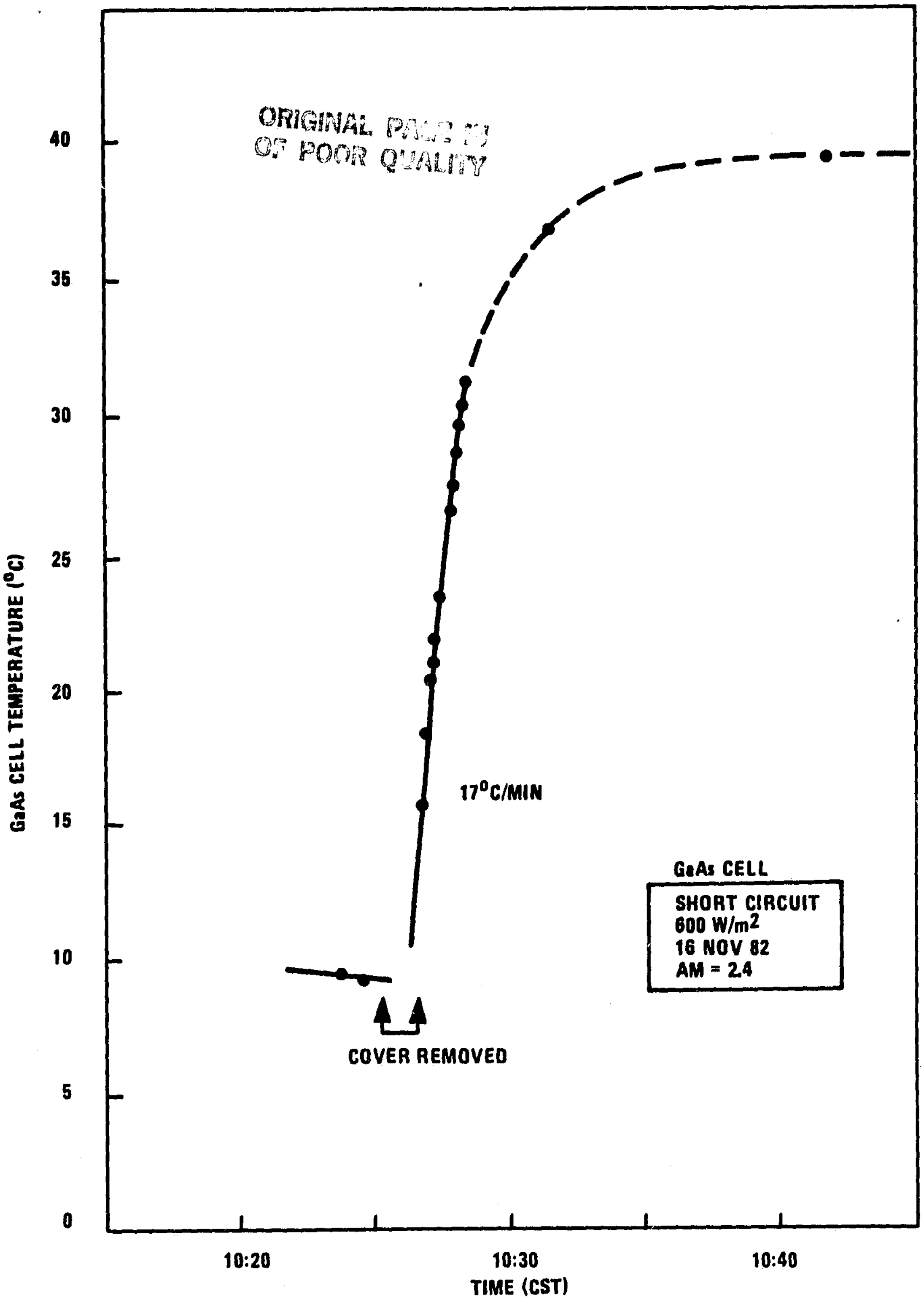

Figure 39. Temperature Rise Rate for the Solar Cells

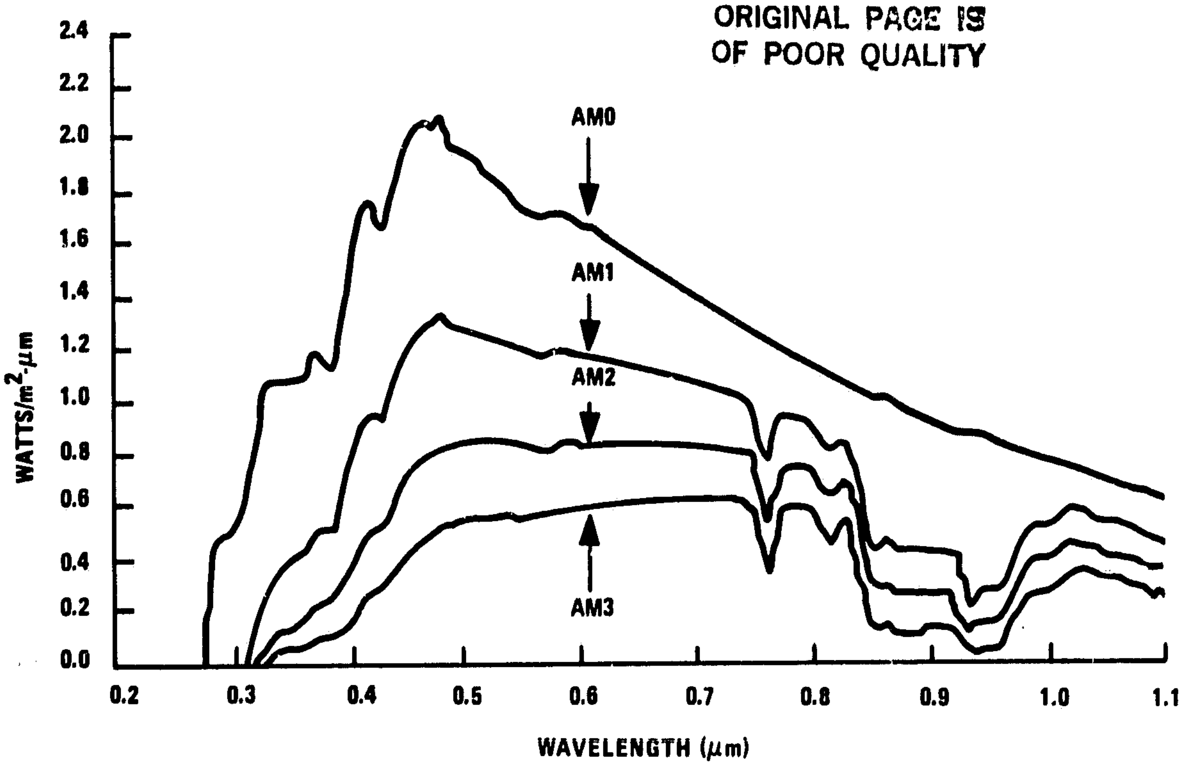

Figure 40. Spectral Intensity vs Air Mass

is apparent why the GaAs cell output is much greater than that of the Si cell. This observation is borne out in both the previously presented experimental data and the calculated values presented in the following paragraphs.

The method of calculating system performance was to piecewise integrate all system parameters over the 0.29- to 1.10-μm spectral range. The spectrum was broken into 82 finite bands each 0.01 μm or 10 nanometers in width and each component property input at the center wavelength. The solar spectrum, mirror reflectances, beamsplitter reflectance and transmission, and solar cell quantum efficiency were all entered into the model at 0.01-μm increments. Because of the large number of equal-width spectral bands, a simple summation of terms produces acceptably accurate results. The accuracy of the input data does not justify more sophisticated curve fitting integration schemes. A sample listing of one computer run is presented in Appendix A. That particular calculation is for the nominal AM2 solar flux case using the measure property data and the best estimates where properties are unavailable. It forms the baseline for comparison of measured versus calculated performance in the following paragraphs.

Comparison of measured versus calculated system efficiency will be presented first. This will be followed by calculated efficiencies with various component modifications all for a nominal AM2 air mass.

The measured data were taken at various times during the day, with the result that, not only was the air mass varying, but the solar intensity varied considerably due to changes in atmospheric scattering and absorption. To place the comparisons on as nearly an equal basis as possible, the calculated cell output was scaled up and down by the ratio, and measured flux divided by AM2 solar constant. No attempt was made to further correct the calculated output based on variations in spectral content.

Table 3 presents the comparison of measured and calculated solar power output. Note that the basis of comparison is the current times voltage product and not the measured power output. The I-V product is nearly independent of the flux level, whereas the maximum power attainable depends on cell-internal resistance, cell temperature, and cell design and flux level. All but temperature can be lumped into one variable called "fill factor," which only depends on flux level, but the cells have not been sufficiently characterized to do that with any accuracy.

ORIGINAL PAGE IS
OF POOR QUALITY

TABLE 3. COMPARISON OF MEASURED AND CALCULATED POWER OUTPUT

Solar Cell	Measured Solar Flux (W/m^2)	Measured I x V (W)	Calculated I x V (W)	Difference (%)
16 NOV '82				
GaAs	569.5	4.67	4.294	+ 8.8
Si	586	0.74	0.477	+55
18 NOV' 82				
GaAs	508.5	4.17	3.834	+ 8.8
Si	536.5	0.68	0.437	+56
No Beam-splitter				
Si	520.5	2.64	3.050	-13.4

The model predicts the performance of the cells very consistently over a range of solar fluxes. The accuracy of predicted GaAs power output is quite good. The Si cell predicted output is much lower than measured. We suspect that a calibration error was undetected. A review of the raw data did not indicate any probable cause for the abnormal differences between measurements and calculations.

For the third case, where the entire sun was concentrated on the Si cell, the measured power was 13% below the calculated value. Five percent of that difference can be attributed to the heating of the cell, as previously mentioned. This close agreement tends to indicate that the large error in previous Si cell power measurements may be an electrical signal offset error, possibly noise, which is a much higher percentage error at low signal level.

To determine possible system efficiencies with the existing solar cells, the maximum efficiences from different conditions were calculated. These results are presented in Table 4 for A) the existing system, B) the existing system without the beamsplitter and only one solar cell, C) a system with perfect optical components, and D) a system with perfect optical components and without a beamsplitter. The Si cell contributes less than 10% of the output of the existing system. When compared to configuration, which has no

TABLE 4. CALCULATED CELL AND SYSTEM EFFICIENCIES*

	Wavelength (μm)		
	0.29-0.90 (%)	0.91-1.10 (%)	Total (%)
A) Existing System			
GaAs	16.6	0	16.6
Si	0.2	1.6	1.8
		Total	= 18.4
B) Existing System-- No Beamsplitter			
GaAs	17.3	0	17.3
or Si	11.03	1.8	12.9
C) Perfect Optics			
GaAs	24.0	0	24.0
Si	0	2.7	2.7
		Total	= 26.6
D) No Beamsplitter + Perfect Optics			
GaAs	24.0	0	24.0
Si	14.9	2.7	17.6

*Assumes a fill factor of unity. Fill factors are typically between 70% and 80%.

beamsplitter losses, the Si cell and beamsplitter only contribute 6% to the net power output. To determine the upper limit of performance, Case C was analyzed. Perfect optics and beamsplitter were assumed. In this case, the Si cell contributed 9.8% of the total output. If each cell was exposed to the sun with perfect mirrors and without beamsplitter, Case D, the GaAs cell would produce 36% more energy than the Si cell. Although the GaAs cell does not utilize the energy in the 0.9- to 1.1-μm range that the Si cell can convert, the 57% higher output voltage more than compensates over the 0.3- to 0.9-μm range. The quantum efficiencies are similar over the 0.3- to 0.9-μm spectral range.

To clarify where the losses occur in the SPV test model, the average optical properties for each of the components were calculated. These results are presented in Table 5. The spectrally weighted average reflectance and/or transmission of each component was calculated by integrating over the given spectral range and comparing the system output with the case having a perfect optical component. Because reflectance varies with wavelengths, it can be shown mathematically that the system performance is not degraded proportionally to the product of the component performance. But the component spectral characteristics do not vary widely over the spectrum, with the result that products of average values provide a good first estimate of performance. For the 0.29- to 0.90-μm band, the product of reflectances is 64%. In Table 4 the ratio of the GaAs cell output Case A, divided by Case C, is 69%, thus proving both points--that the product is useful, but not exact. From the data presented in Table 5, it is obvious that the mirrors and the CPC require improvement. The beamsplitter could also be improved by reducing its shortwave absorption. Considering the difficulties encountered achieving high component performances, every consideration should be given to reducing the number of components in the optical path.

TABLE 5. SPV COMPONENT OPTICAL PROPERTIES[*]

	Wavelength (μm)		
	0.29 to 0.9	0.91 to 1.1	0.29 to 1.1
Primary Mirror Reflectance[**]	0.887	0.871	0.884
Beamsplitter Transmission	0.012	0.895	--
Beamsplitter Reflectance	0.926	0.091	--
Beamsplitter Absorption	0.062	0.014	0.555
CPC Reflectance[†]	0.88	0.90	

[*] Evaluated by integration over the solar spectrum, AM2 $\alpha = 0.66$, $\beta = 0.17$

[**] Secondary mirror reflectance assumed identical to primary mirror

[†] Estimated based on 40% of energy having one reflection from CPC and handbook value of bright nickel reflectance

CONCLUSIONS

The SPV concept shows promise of making small improvements in solar-to-electric conversion efficiency. There cannot be any dramatic gains in conversion efficiency using GaAs and Si cells because the Si cell sees only 10% of the energy that the GaAs does not use. Should good blue-responding AlGaAs solar cells become available in the future, an AlGaAs and Si spectrophotovoltaic system may appear attractive, especially in an AMO environment.

RECOMMENDATIONS

The SPV model should be further tested to quantify the fill factor roll-off with increasing solar flux. The heat rejection problem needs further investigation, particularly when considering larger aperture systems.

We recommend that a comprehensive series of high-altitude field tests and further system design work be performed when better AlGaAs solar cells become available (i.e., cells with higher quantum efficiency and better blue response).

REFERENCES

1. Mecherikunnel, Ann T. and Richmond, Joseph C., "Solar Spectral Irradiance at Ground Level," Proceedings of the Institute of Environmental Sciences Seminar on Testings Solar Energy Materials and Systems, May 22-24, 1978.

2. Kamath, S.; Knechtli, R.C.; Schwartz, S.; and Wolff, G., "GaAs Concentrator Photovoltaic Power System Feasibility Investigation," Contract No. F33615-76-C-2142, Hughes Aircraft Company, El Segundo, California, December 1977.

APPENDIX A

SAMPLE SYSTEM ANALYSIS LISTING

PRECEDING PAGE BLANK NOT FILMED

APPENDIX A

SAMPLE SYSTEM ANALYSIS LISTING

The following computer output listing is a sample calculation of the SPV output based on the assumption of an AM2 atmosphere and the measured cell and concentrator component data. Table A-1 identifies the printout columns and their interrelationships.

At the bottom of the listing column summations and the spectral energy content applicable to the GaAs and Si cells are listed. The solar data are taken from Reference 1, assuming an AM2 spectrum with scattering and absorption coefficients of $\alpha = 0.66$ and $\beta = 0.17$.

TABLE A-1. PRINTOUT COLUMNS AND THEIR INTERRELATIONSHIPS

Printout Column	Contents
A	Wavelength in nanometers
B	Spectral intensity in W/nm - m^2
C	Gallium arsenide solar cell spectral quantum efficiency (electrons per photon)
D	Silicon solar cell spectral quantum efficiency
E	Beamsplitter spectral transmission
F	Beamsplitter spectral reflectance
G	Primary mirror spectral reflectance
H	GaAs cell spectral current amp/nm - m^2 (A × B × C × F × G^2 × 0.88 × 0.0008065) Note: CPC effective reflectance is 0.88
I	Si cell spectral current amp/nm - m^2 (A × B × D × E × G^2 × 0.90 × 0.0008065)
J	Summation of GaAs cell current from λ_1 = 290 nm to λ(n) in amp/m^2 [J(n) = 10 × H(n) + J(n - 1)]
K	Summation of Si cell current from λ_1 = 290 nm to λ(n) in amp/m^2 [K(n) = 10 × I(n) + K(n - 1)]
L	Summation of GaAs cell power output from λ_1 = 290 nm to λ(n) L(n) = 1.1 J(n)
M	Summation of Si cell power output from λ_1 = 290 nm to λ(n) M(n) = 0.7 K(n)

A	B	C	D	E	F	G	H	I	J	K	L	M
WAVE LENGTH	W/NM M2 AM2	GAAS Q-EFF	SI Q-EFF	BEAM-SPLT TRANS	BEAM-SPLT REFL	MIRRO REFL	GA-I /NM-M2	SI-I /NM-M2	GA-SUM I/M2	SI-SU I/M2	GAAS W/M2	SI W/M2
290	0	0	0	0	.4	.58	0	0	0	0	0	0
300	0	0	0	0	.4	.6	0	0	0	0	0	0
310	.001	0	0	0	.4	.62	0	0	0	0	0	0
320	.034	0	0	0	.4	.64	0	0	0	0	0	0
330	.073	0	0	0	.4	.66	0	0	0	0	0	0
340	.123	0	0	0	.4	.68	0	0	0	0	0	0
350	.15	0	.0031	.0005	.4	.7	0	3.E-8	0	3.E-7	0	2.E-7
360	.177	0	.0016	.0354	.4	.72	0	1.E-6	0	1.E-5	0	9.E-6
370	.222	0	.0329	.0579	.3398	.74	0	6.E-5	0	6.E-4	0	4.E-4
380	.239	0	.0355	.0234	.5232	.76	0	3.E-5	0	10E-4	0	7.E-4
390	.258	.076	.0499	.0242	.765	.78	.0025	5.E-5	.0253	.0015	.0278	.0010
400	.37	.1	.101	.0091	.6969	.803	.0047	6.E-5	.0725	.0021	.0797	.0015
410	.485	.13	.138	.0723	.8666	.82	.0107	10E-4	.1794	.0118	.1973	.0083
420	.516	.119	.177	.0108	.9106	.834	.0116	2.E-4	.2953	.0139	.3248	.0097
430	.517	.163	.227	.0021	.8811	.83	.0156	5.E-5	.4514	.0144	.4965	.0101
440	.609	.226	.271	.0015	.8558	.84	.0260	6.E-5	.7109	.0150	.7820	.0105
450	.721	.278	.318	.0005	.8617	.84	.0389	3.E-5	1.100	.0153	1.210	.0107
460	.769	.364	.372	.0005	.9164	.84	.0591	3.E-5	1.691	.0156	1.860	.0109
470	.783	.417	.415	.0005	.926	.839	.0710	4.E-5	2.401	.0160	2.641	.0112
480	.827	.479	.456	.0005	.9396	.839	.0893	5.E-5	3.294	.0164	3.623	.0115
490	.805	.559	.494	.0005	.91	.839	.1002	5.E-5	4.296	.0169	4.726	.0119
500	.829	.641	.529	.0005	.9088	.84	.1209	6.E-5	5.505	.0175	6.056	.0123
510	.818	.707	.567	.0005	.9253	.847	.1390	6.E-5	6.895	.0181	7.584	.0127
520	.811	.742	.598	.0005	.9569	.853	.1546	7.E-5	8.441	.0188	9.285	.0131
530	.83	.756	.614	.0005	.8788	.86	.1534	7.E-5	9.975	.0195	10.97	.0137
540	.817	.76	.633	0	.9814	.866	.1751	0	11.73	.0195	12.90	.0137
550	.805	.762	.65	.0006	.9671	.87	.1753	9.E-5	13.48	.0205	14.83	.0143
560	.8	.764	.664	.0005	.9092	.875	.1691	8.E-5	15.17	.0213	16.69	.0149
570	.818	.775	.674	.0005	.9734	.883	.1946	9.E-5	17.12	.0222	18.83	.0155

ORIGINAL PAGE IS
OF POOR QUALITY

```
  580  .829  .775  .685      0 .9516  .887 .1980      0 19.1  .[illegible]22 21.01 .0155
  590  .831  .782  .696      0 .9559   .89 .2060      0 21.16 .0222 23.27 .0155
  600  .824  .784  .701  .0005 .9734  .892 .2131 1.E-4 23.29 .0232 25.62 .0162
  610  .827  .765  .701  .0005 .9183  .894 .2063 1.E-4 25.35 .0242 27.89 .0169
  620  .828  .782  .716      0 .9814  .898 .2255      0 27.61 .0242 30.37 .0169
  630   .83  .779  .738  .0005 .9815    .9 .2298 1.E-4 29.90 .0253 32.89 .0177
  640  .834  .801  .759  .0053 .9322  .904 .2312 .0013 32.22 .0381 35.44 .0266
  650  .834  .803  .762  .0005 .9645  .907 .2451 1.E-4 34.67 .0393 38.13 .0275
  660  .833  .802  .771  .0007  .992  .908 .2559 2.E-4 37.23 .0411 40.95 .0288
  670  .828   .79  .769  .0046 .9936   .91 .2559 .0012 39.79 .0529 43.76 .0370
  680  .824  .792  .772  .0015  .958  .912 .2510 4.E-4 42.29 .0568 46.52 .0398
  690  .821  .784  .766  .0005 .9568  .915 .2525 1.E-4 44.82 .0581 49.30 .0407
  700  .814  .772  .776  .0007 .9777  .917 .2567 2.E-4 47.39 .0600 52.12 .0420
  710  .805  .768  .765  .0005 .9751  .919 .2566 1.E-4 49.95 .0613 54.95 .0429
  720  .794  .759   .77   .001 .9744  .922 .2551 3.E-4 52.50 .0641 57.75 .0448
  730  .786  .753  .762   .001 .9762  .924 .2556 3.E-4 55.06 .0668 60.56 .0467
  740  .773  .745   .76   .001 .9793  .926 .2540 3.E-4 57.60 .0695 63.36 .0486
  750  .764  .737  .732   .001 .9755   .93 .2529 3.E-4 60.13 .0721 66.14 .0505
  760  .536  .732  .723  .0001 .9797  .932 .1801 2.E-5 61.93 .0723 66.12 .0506
  770  .745  .729  .723   .002 .9741  .936 .2533 5.E-4 64.46 .0776 70.91 .0543
  780  .734  .729  .725  .0021   .98   .94 .2565 6.E-4 67.03 .0832 73.73 .0582
  790  .723  .735  .722  .0022 .9745  .942 .2576 6.E-4 69.60 .0890 76.56 .0623
  800  .713  .739  .728  .0078 .9761  .944 .2602 .0021 72.20 .1099 79.42 .0770
  810  .625  .741  .728  .0188 .9749  .946 .2323 .0045 74.53 .1550 81.98 .1085
  820  .664  .742  .734  .0241 .9739  .946 .2499 .0063 77.03 .2175 84.73 .1523
  830  .677  .737  .728  .0297   .97  .945 .2546 .0079 79.57 .2963 87.53 .2074
  840  .489  .736  .728   .041   .95  .942 .1809 .0079 81.38 .3752 89.52 .2627
  850   .28  .729  .724  .0663   .93  .939 .1010 .0073 82.39 .4484 90.63 .3138
  860  .301  .718  .722  .0887   .91  .934 .1047 .0105 83.44 .5533 91.78 .3873
  870   .26  .691  .715  .1137   .88  .928 .0841 .0115 84.28 .6683 92.71 .4678
  880  .259  .357  .714  .1544   .84  .921 .0411 .0155 84.69 .8230 93.16 .5761
  890  .262  .081  .708  .2428   .75  .916 .0084 .0244 84.77 1.067 93.25 .7470
  900  .265  .026  .706  .3373  .643  .909 .0023 .0341 84.80 1.408 93.28 .9854
  910  .275  .004  .702  .4883  .492  .901 3.E-4 .0505 84.80 1.913 93.28 1.339
  920  .208     0  .695  .6539  .326  .898     0 .0509 84.80 2.422 93.28 1.696
  930    .1     0  .701  .7817  .198  .893     0 .0295 84.80 2.717 93.28 1.902
  940  .164     0  .701  .8485  .132  .888     0 .0525 84.80 3.242 93.28 2.269
  950  .153     0  .694  .8936  .086  .885     0 .0512 84.80 3.754 93.28 2.628
  960  .182     0  .677   .924  .056  .884     0 .0620 84.80 4.374 93.28 3.062
  970  .296     0  .658   .933   .06   .88     0 .0991 84.80 5.365 93.28 3.756
  980  .388     0  .639  .9298 .0553  .876     0 .1258 84.80 6.624 93.28 4.637
  990  .385     0  .623  .9294 .0513  .874     0 .1224 84.80 7.847 93.28 5.493
 1000  .407     0  .583  .9351 .0335  .872     0 .1225 84.80 9.072 93.28 6.350
 1010  .429     0  .522  .9365   .06   .87     0 .1164 84.80 10.24 93.28 7.165
 1020  .444     0  .452  .9149 .0788  .868     0 .1024 84.80 11.26 93.28 7.882
 1030  .431     0  .391   .914 .0673  .867     0 .0866 84.80 12.13 93.28 8.488
 1040  .417     0   .31  .9252 .0631  .864     0 .0674 84.80 12.80 93.28 8.960
 1050  .403     0  .238   .937   .06  .863     0 .0510 84.80 13.31 93.28 9.317
 1060  .389     0  .182   .936   .06  .861     0 .0378 84.80 13.69 93.28 9.581
 1070  .375     0  .141   .932 .0449   .86     0 .0283 84.80 13.97 93.28 9.779
 1080  .361     0  .111  .9305  .069  .858     0 .0215 84.80 14.19 93.28 9.930
 1090  .343     0 .0649  .9246 .0719  .857     0 .0120 84.80 14.31 93.28 10.01
 1100  .374     0 .0478  .9107  .059  .857     0 .0095 84.80 14.40 93.28 10.08

TOTAL= 429.4                              84.80 14.40 84.80 14.40 93.28 10.08
.29-.9 364.2
.9-1.1 65.24

ALPHA=   .66
BETA =   .17
```

APPENDIX B

OPTICAL AND ELECTRIC COMPONENT DRAWINGS

APPENDIX B

OPTICAL AND ELECTRIC COMPONENT DRAWINGS

The six drawings in Appendix B define the optical surfaces, their relationship to each other, and the electrical wiring system. The wiring diagram identifies individual pin connections, lead wire lengths, and the solar cell variable resistance box.

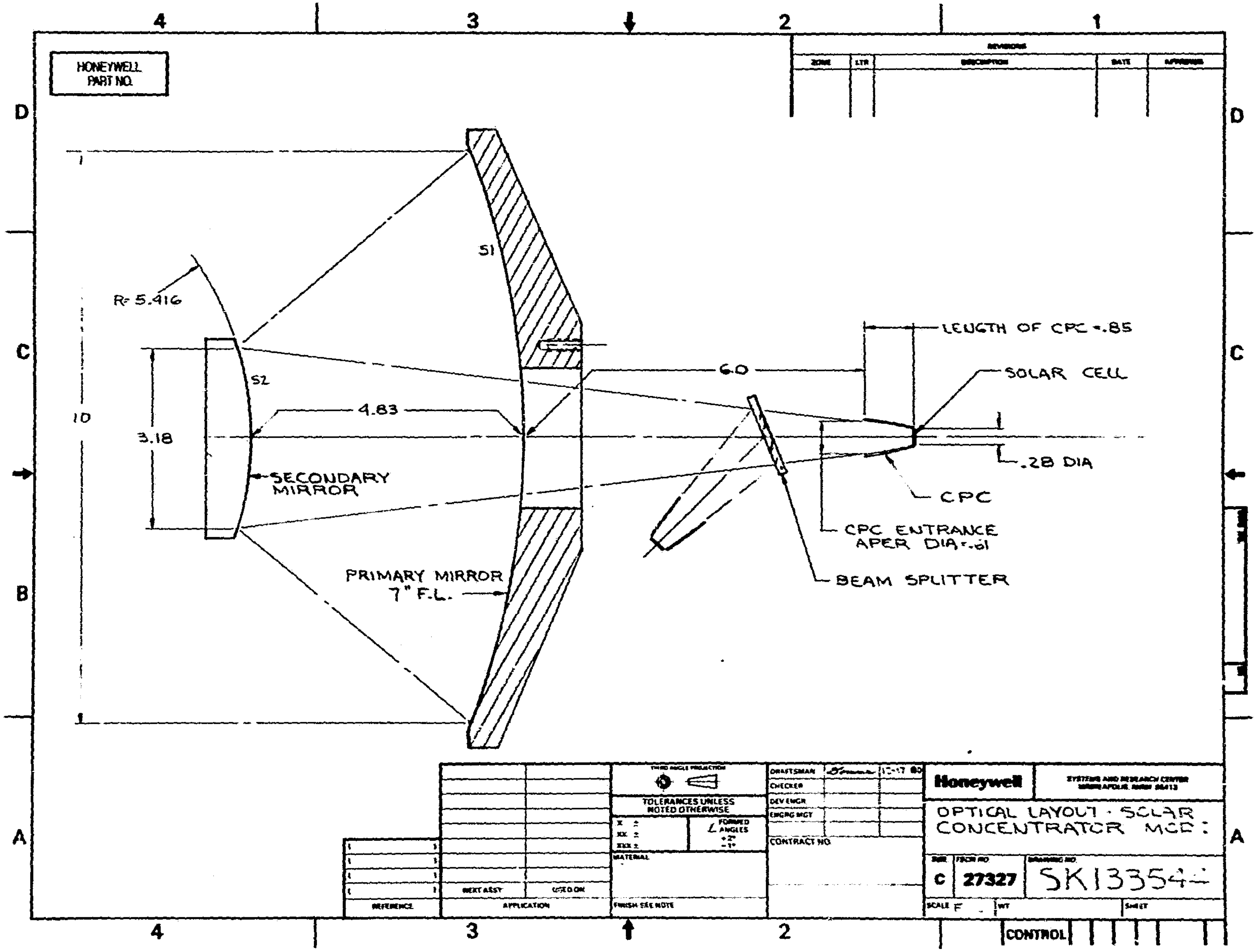
HONEYWELL PART NO.
REVISIONS
ZONE
LTR
DESCRIPTION
DATE
APPROVED
R=5.416
10
3.18
S2
SECONDARY MIRROR
4.83
S1
PRIMARY MIRROR 7" F.L.
6.0
LENGTH OF CPC=.85
SOLAR CELL
.28 DIA
CPC
CPC ENTRANCE APER DIA=.61
BEAM SPLITTER
REFERENCE
NEXT ASSY
USED ON
APPLICATION
THIRD ANGLE PROJECTION
TOLERANCES UNLESS NOTED OTHERWISE
X ±
XX ±
XXX ±
FORMED ∠ ANGLES +2° −1°
MATERIAL
FINISH SEE NOTE
DRAFTSMAN
12-17 80
CHECKER
DEV ENGR
ENGRG MGT
CONTRACT NO.
Honeywell
SYSTEMS AND RESEARCH CENTER MINNEAPOLIS, MINN 55413
OPTICAL LAYOUT · SOLAR CONCENTRATOR MOD:
SIZE C
FSCM NO 27327
DRAWING NO SK13354-
SCALE F
WT
SHEET
CONTROL
4
3
2
1
D
C
B
A

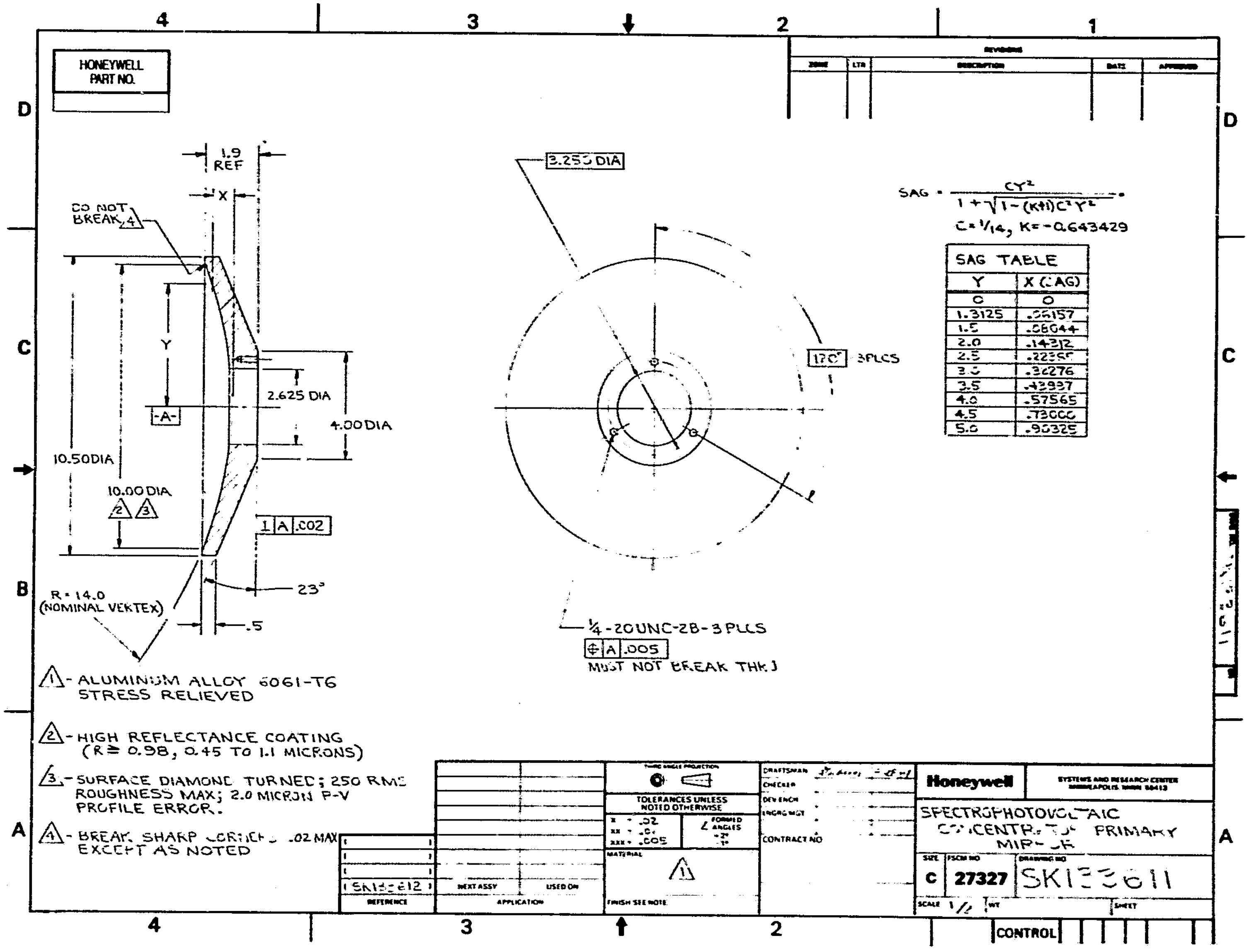

$$SAG = \frac{CY^2}{1+\sqrt{1-(K+1)C^2Y^2}}$$

$C = 1/14$, $K = -0.643429$

SAG TABLE	
Y	X (SAG)
0	0
1.3125	.06157
1.5	.08044
2.0	.14312
2.5	.22355
3.0	.32276
3.5	.43937
4.0	.57565
4.5	.73066
5.0	.90325

1 - ALUMINUM ALLOY 6061-T6 STRESS RELIEVED

2 - HIGH REFLECTANCE COATING ($R \geq 0.98$, 0.45 TO 1.1 MICRONS)

3 - SURFACE DIAMOND TURNED; 250 RMS ROUGHNESS MAX; 2.0 MICRON P-V PROFILE ERROR.

4 - BREAK SHARP CORNERS .02 MAX EXCEPT AS NOTED

Honeywell

SYSTEMS AND RESEARCH CENTER
MINNEAPOLIS, MINN 55413

SPECTROPHOTOVOLTAIC
CONCENTRATOR PRIMARY
MIRROR

SIZE C
FSCM NO 27327
DRAWING NO SK133611
SCALE 1/2

ORIGINAL PAGE IS
OF POOR QUALITY

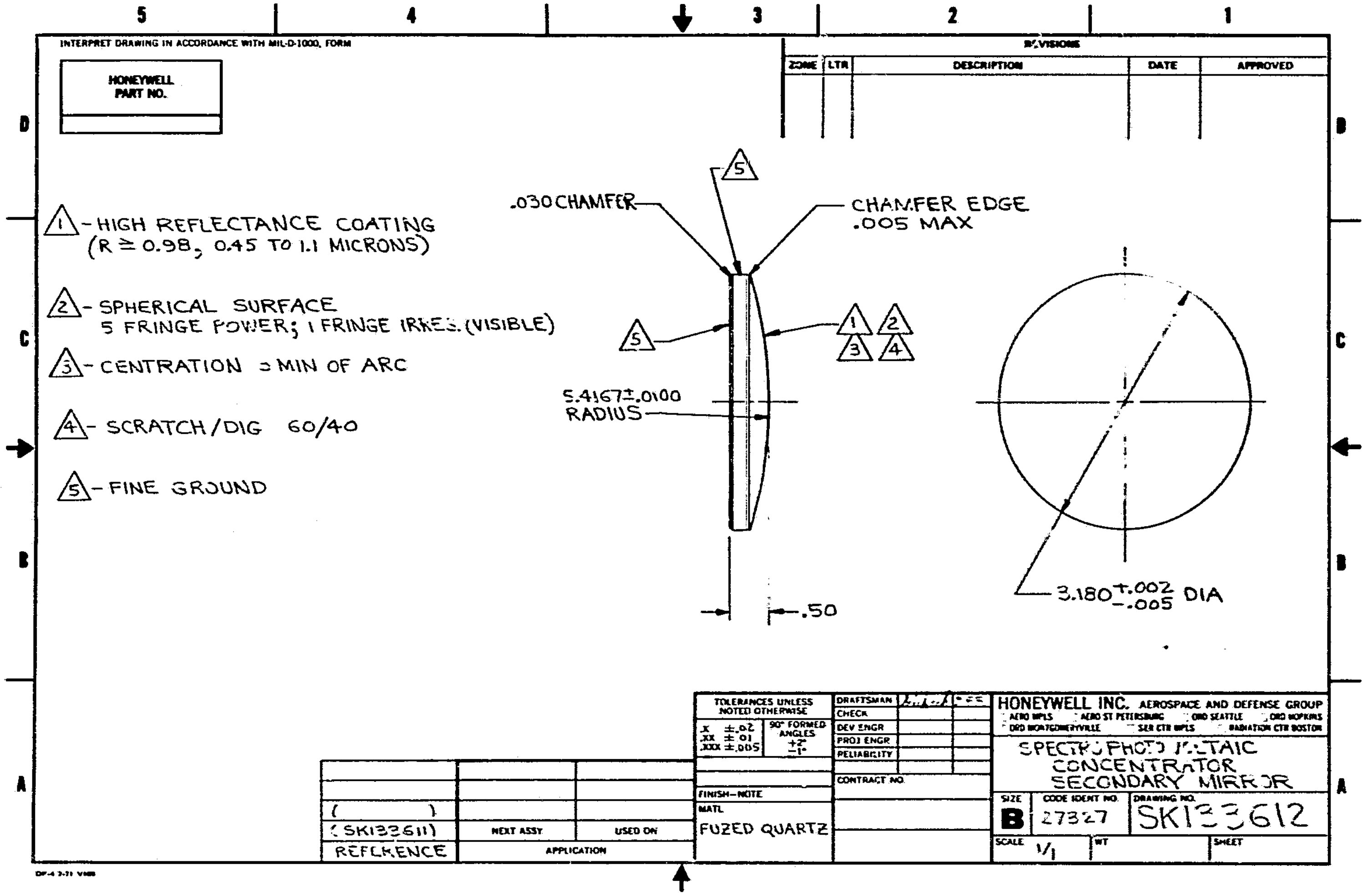

HONEYWELL
PART NO.

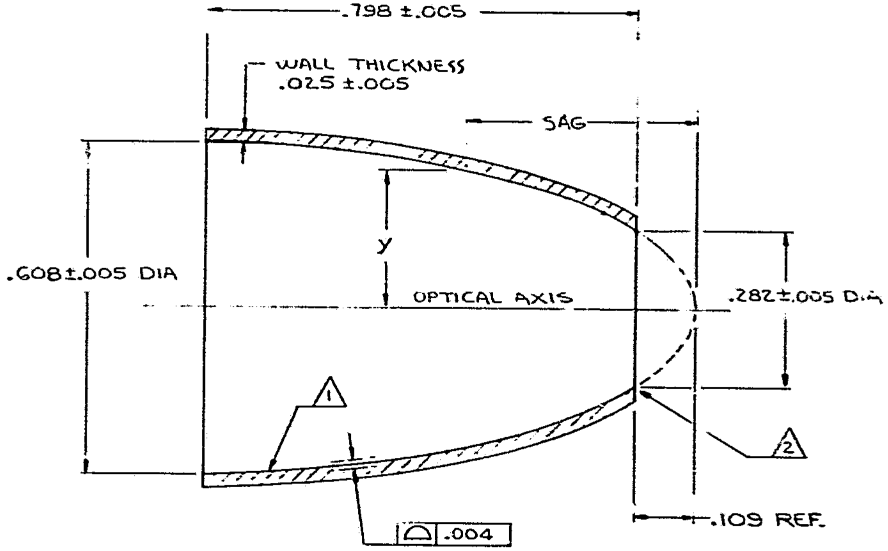

$\frac{1}{C}$ = RADIUS: -.096397

K = CONIC CONSTANT: -.89978

$$SAG = \frac{Cy^2}{1+\sqrt{1-(K+1)C^2y^2}}$$

Y	SAG
.141	-.109
.150	-.125
.160	-.143
.170	-.164
.180	-.186
.190	-.210
.200	-.237
.210	-.265
.220	-.297
.230	-.332
.240	-.370
.250	-.413
.260	-.461
.270	-.517
.280	-.584
.290	-.669
.300	-.797
.304	-.907

2\ CORNER SHARP AND FREE OF BURRS

1\ REFLECTIVE COATING - ENHANCED ALUMINUM.

NEXT ASSY | USED ON
APPLICATION
REFERENCE

THIRD ANGLE PROJECTION

TOLERANCES UNLESS NOTED OTHERWISE
X ±
XX ±
XXX ±
∠ FORMED ANGLES ±2° ±1°
MATERIAL
FINISH SEE NOTE

DRAFTSMAN 9-2-81
CHECKER
DEV ENGR
ENGRG MGT
CONTRACT NO

Honeywell
SYSTEMS AND RESEARCH CENTER
MINNEAPOLIS, MINN 55413

COMPOUND PARABOLIC
CONCENTRATOR

SIZE C | FSCM NO 27327 | DRAWING NO SK133609
SCALE 8X | WT | SHEET

CONTROL

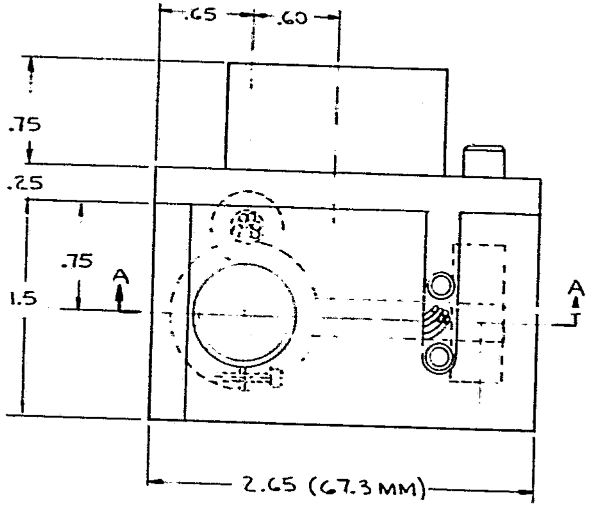
.65
.60
.75
.25
.75
1.5
A
A
2.65 (67.3 MM)

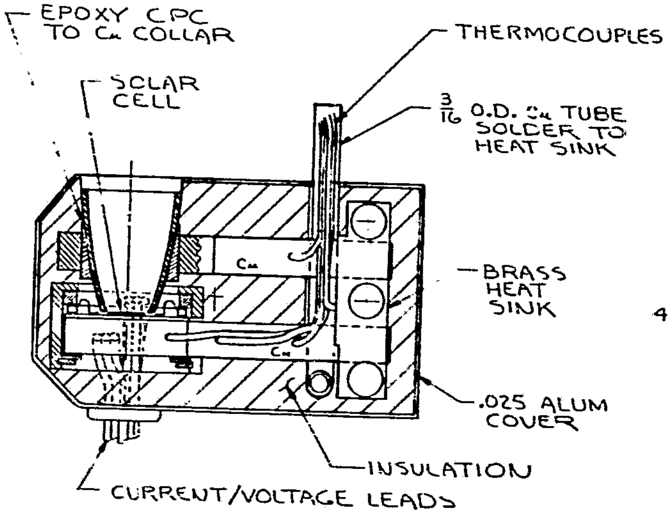
EPOXY CPC TO Cu COLLAR
SOLAR CELL
THERMOCOUPLES
$\frac{3}{16}$ O.D. Cu TUBE SOLDER TO HEAT SINK
BRASS HEAT SINK
Cu
Cu
.025 ALUM COVER
INSULATION
CURRENT/VOLTAGE LEADS

SECTION A-A

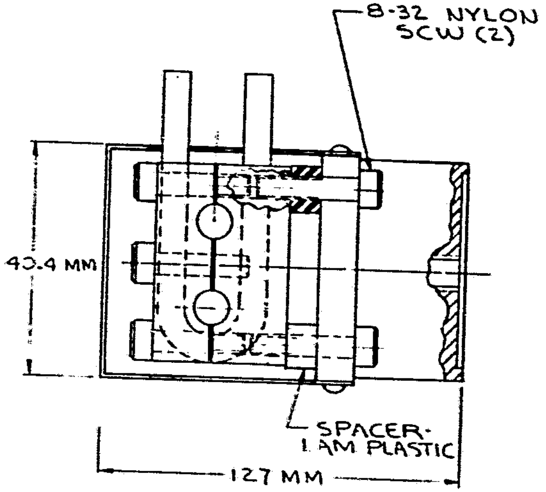
8-32 NYLON SCW (2)
40.4 MM
SPACER-LAM PLASTIC
127 MM

ORIGINAL PAGE IS
OF POOR QUALITY